RSC Advances

PAPER

View Article Online
View Journal | View Issue

Cite this: *RSC Adv.*, 2026, **16**, 9455

Comprehensive evaluation of synthesized dual-headed Gemini ionic liquids as protective inhibitors for carbon steel in aerated 3.0 M HCl: electrochemical and theoretical approaches

Reda Abdel-Hameed,[a] Odeh A. O. Alshammari,[b] Bader Huwaimel,[c] Eshraqa Ali,[a] Kaseb D. Alanazi,[b] Ayham Ali Bani Essa,[b] Ahmed H. Tantawy,*[d] Kamal A. Soliman[d] and Doaa F. Seyam[d]

Carbon steel readily corrodes in acidic environments, particularly in HCl, where corrosion severity depends on acid concentration, exposure time, and temperature. In this study, three novel ionic liquid-based Gemini cationic surfactants were synthesized and structurally characterized using various spectroscopic techniques. Their effectiveness as corrosion inhibitors for carbon steel in aerated 3.0 M HCl was evaluated *via* weight-loss measurements across multiple temperatures, potentiodynamic polarization (PDP), and electrochemical impedance spectroscopy (EIS). The surfactants exhibited excellent inhibition performance, with GSE-12 achieving up to 98.00% efficiency. EIS results in the presence of GSE revealed a two-time constant (R_S-2RC) response, indicating protective film formation on the steel surface. Adsorption followed the Langmuir isotherm and increased the activation energy (E_a), enthalpy (ΔH^*), and entropy (ΔS^*) of the corrosion process. Inhibition efficiency improved with temperature up to 50 °C, reflecting the thermal stability of the inhibitors. The Gibbs free energy of adsorption for GSE-12 was −59.49 kJ mol^{-1}, suggesting a mixed physisorption–chemisorption mechanism. All compounds acted as mixed-type inhibitors with cathodic dominance and showed resistance against time. Computational studies using density functional theory (DFT) and Monte Carlo simulations (MCS) supported the experimental findings, showing that GSE-12 has superior electronic properties and stronger adsorption on the Fe(110) surface compared to GSE-14 and GSE-16, aligning with its enhanced inhibition performance.

Received 14th November 2025
Accepted 13th February 2026

DOI: 10.1039/d5ra08814c

rsc.li/rsc-advances

1 Introduction

Carbon steel is highly susceptible to rusting in aerated acidic conditions, which is a frequent occurrence in many industrial settings, and its resistance to corrosion in industries with high acidic environments is a significant problem. The main causes of the rapid corrosion are acidic species and dissolved oxygen, which serve as cathodic depolarizers and encourage electrochemical reactions that break down the metal. Carbon steel naturally deteriorates in these conditions, causing serious corrosion problems.[1] Corrosion can also be affected by the corrosive solution's flow rate. Increased flow rates can hasten corrosion by speeding up the pace at which acid and oxygen reach the metal surface.[2] In some building situations, carbon steel structures may be subjected to acidic conditions. Carbon steel may corrode more quickly in pH-adjusted solutions in geothermal brines. Dew condensations, which are frequently acidic, can seriously harm atmospheric corrosion. One of the main causes of pipeline failures in offshore gas pipelines is corrosion.[3]

The rate of corrosion can be considerably decreased by adding corrosion inhibitors to acidic fluids. By changing the electrochemical reactions or creating a protective layer on the metal surface, chemical inhibitors can assist in lowering the rates of corrosion.[4] Surface-active substances can act as effective corrosion inhibitors, particularly in acidic solutions like HCl, by adsorbing onto the metal surface and creating a protective barrier. This adsorption can be influenced by factors like surfactant type, concentration, and solution temperature. Additionally, other surface-active substances, such as organic compounds, Gemini surfactants,[5,6] ionic surfactants, and non-ionic surfactants,[7] are also described as potent inhibitors that prevent corrosion. They have a lot of advantages including low toxicity, low cost, high inhibition efficiency, and ease of

[a]*Basic Science Department, Preparatory Year, University of Ha'il, Hail, 81442, Saudi Arabia*

[b]*Department of Chemistry, College of Science, University of Ha'il, 81442 Hail, Saudi Arabia*

[c]*Department of Pharmaceutical Chemistry, College of Pharmacy, University of Ha'il, Hail 81442, Saudi Arabia*

[d]*Chemistry Department, Faculty of Science, Benha University, Benha-3518, Egypt. E-mail: ahmed.tantawy@fsc.bu.edu.eg*

manufacturing. The high surface activity of these organic corrosion inhibitors arises from their strong adsorption onto metal interfaces through physicochemical interactions.[8] The length of the hydrophobic chain of the surfactant inhibitors controls their migration from the bulk solution to the interface; also, the hydrophobic tails form a barrier film that separates the metal surface from the corrosive solution. Usually, the surfactant's head group (hydrophilic head group) contains a functional group that is rich in electrons and contributes to the adsorption process with the metal's d-orbital. Bi-functional amphiphilic surfactants known as Gemini surfactants (GS) have two polar head groups and two hydrophobic tails joined through a spacer. Gemini surfactants, with their unique molecular structure, have shown particular promise in this area due to their high surface activity and ability to reduce surface tension. Because Gemini surfactants have two hydrophilic and two hydrophobic groups, their adsorption on metal surfaces is more complex than that of ordinary surfactants.[9]

Most of the studies on organic compounds' ability to inhibit corrosion was carried out in carbon steel/1.0 M HCl[10–15] and to a less extent carbon steel/0.5 M HCl[5,16,17] solution systems. Although some researches were conducted for a stainless steel/3 M HCl solution system, as Kaczerewska *et al.*[18] who have succeeded in inhibiting corrosion of stainless steel in 3 M HCl showing 98% inhibiting efficiency at 3 mM of 12-MOH-O-MOH-12. Also, Marta Pakiet *et al.*[19] inhibited AISI 304 stainless steel from corrosion in 3 M HCl with 0.015 mM of TMTN12Br reaching efficiency of 95%. And before them, with the help of some quinolines, Abdel-Aal and Morad[20] inhibited, with efficiency of 69.1%, the corrosion of mild steel in deaerated 3 M HCl solution. However, to our knowledge, there is no published work dealing with a carbon steel/3 M HCl aerated solution system. A typical concentration for industrial acid pickling and oil well acidizing is 3 M HCl. Current protection measures are frequently based on less aggressive models, which could result in under-design in actual aerated industrial environments due to the lack of aerated-specific data at this concentration. For carbon steel protection in aerated 3 M HCl, there is a noticeable dearth of thorough, peer-reviewed research. By addressing this work, a new foundation for comprehending dual-pathway cathodic reactions in hyperacidic fluids is established.

Finally, Density Functional Theory and Monte Carlo Simulations were employed to gain detailed insights into the corrosion inhibition performance of the investigated molecules by linking their structural and electronic properties to their adsorption behaviour on metallic surfaces. Although experimental investigations are indispensable for elucidating corrosion inhibition mechanisms and quantifying inhibition efficiencies, they can be costly and time-consuming, often requiring sophisticated instrumentation and lengthy protocols. In contrast, computational modelling offers a powerful and efficient alternative, enabling the prediction of key molecular reactivity descriptors.[21–26] Monte Carlo simulations further complement DFT by enabling exploration of adsorption configurational space and identifying the most energetically favourable adsorption geometries under realistic conditions.[27–30] Together, this integrated computational approach provides chemists and materials scientists with a cost-effective, predictive framework for designing and optimizing new corrosion inhibitors.[31]

Therefore, in this study, three novel ionic liquid-based Gemini cationic surfactants were synthesized, and their chemical structures were elucidated using various spectroscopic techniques. Both chemical (weight loss method) and electrochemical techniques including the potentio-dynamic polarization (PDP) and electrochemical impedance spectroscopy (EIS) will be used to determine the inhibition efficiency. Furthermore, a combined computational strategy is adopted to elucidate the inhibition mechanism at the molecular level. Monte Carlo (MC) simulations were used to compute adsorption energies and identify the most stable inhibitor–surface configurations, while density functional theory (DFT) provided electronic-structure descriptors that directly correlate with the observed inhibition activity. Additionally, the anticorrosive effect will be confirmed through scanning electron microscopy (SEM), energy-dispersive X-ray spectroscopy (EDX), and Fourier Transform Infrared Spectroscopy (FTIR) of the carbon steel surface.

2 Experimental methodologies

2.1 Materials

Chloroacetic acid, diethylene glycol, *p*-toluenesulfonic acid (PTSA), and 3-(*N*,*N*-dimethylamino)-1-propylamine (99.1%) were supplied by Sigma-Aldrich Chemicals Co. In Cairo, Egypt, we purchased hexadecenoic, tetradecanoic, and dodecanoic acids from Algomhoria Chemical Co. Diethyl ether, methanol, dry toluene, and sodium sulphate anhydrous were provided by Al-Nasr Chemicals. No further purification was required because all required reagents and solvents were employed precisely as specified. The generated compounds' FTIR spectra were measured as liquid or solid (ATR) using a Thermos Nicolet iS10 FTIR spectrophotometer, Benha University, Egypt. Tetramethyl silane (TMS) was utilized as an internal reference, and NMR spectra were performed using a Bruker Avance (III) 400 MHz signal (Switzerland) with (128) scans at 298 K in DMSO-d_6 as the solvent.

2.2 Synthesis

2.2.1 Preparation of *N*-(3-(dimethylamino)propyl)alkanamides (1a–c). In three separate flasks, *N*,*N*-dimethylpropane-1,3-diamine (10.18 g, 0.1 mol), different fatty acids (0.1 mol each; dodecanoic, tetradecanoic, and hexadecenoic acids), and *p*-toluenesulfonic acid (PTSA, 1 mol%, 0.171 g) were combined. A dean-Stark trap was used to reflux the mixture until the accurate water quantity (0.1 mol) was removed. The reaction mixture was neutralized by the addition of an aqueous $NaHCO_3$ solution to remove unreacted acids, followed by washing with distilled water, drying over anhydrous Na_2SO_4, and filtration. The target compounds, *N*-(3-(dimethylamino)propyl)alkanamides (**1a–c**), were obtained in varying yields and colors after removal of excess toluene using a rotary evaporator at 70–80 °C under reduced pressure.

*2.2.1.1 N-(3-(Dimethylamino)propyl)alkanamide (**1a–c**).* Yellow color; yield = 89%; mp = 94 °C. FT-IR (ATR) ν/cm^{-1}; 1652 (νC=O amide), 2849–2918 (νCH aliphatic fatty chain), 3339 (νNH stretching) (**1a**). Yellowish white color; yield = 90%; mp = 101 °C. FT-IR (ATR) ν/cm^{-1}; 3311 (νNH stretching), 2849–2918 (νCH aliphatic fatty chain), 1652 (νC=O amide) (**1b**). White color; yield = 85%; mp = 110 °C. FT-IR (ATR) ν/cm^{-1}; 1635 (νC=O amide), 2852–2916 (νCH aliphatic fatty chain), 3315 (νNH stretching) (**1c**) (Fig. S2).

2.2.2 Synthesis of oxybis(ethane-2,1-diyl) bis(2-chloroacetate) (2). Diethylene glycol (5.3 g, 0.05 mol) was mixed with chloroacetic acid (10.34 g, 0.11 mol) in 45 mL of toluene in the presence of *p*-toluenesulfonic acid (PTSA, 1 mol%). The reaction mixture was then refluxed to remove the required amount of water. The reaction mixture was neutralized by adding an aqueous $NaHCO_3$ solution, followed by two washes with distilled water, drying over anhydrous Na_2SO_4, and filtration, yielding the desired diester compound (**2**). The rotary evaporator system was utilized to evaporate the excess solvent (toluene) at a temperature of 70–80 °C under reduced pressure, generating a yellowish viscous liquid.

*2.2.2.1 Oxybis(ethane-2,1-diyl) bis(2-chloroacetate) (**2**).* Whitish yellow semi solid; yield = 94%. FT-IR (ATR) ν/cm^{-1}; 2848–2954 (νCH aliphatic CH_2), 1738 (νC=O ester), 1127 (νC–O, ether) and disappear of aliphatic OH group. ^{1}H NMR (500 MHz, $CDCl_3$) δ: 4.32–4.28 (m, 4H), 4.07 (s, 4H), 3.70–3.65 (m, 4H). ^{13}C NMR (101 MHz, $CDCl_3$) δ: 173.05, 67.43, 62.80, 37.91 (Fig. S1).

2.2.3 Synthesis of ionic liquids-based Gemini cationic surfactants (3a–c). Three separate solutions of compound **2** (20 mmol) in 25 mL of acetonitrile were prepared. Then, solutions of **1a–c** (40 mmol each) in 25 mL of acetonitrile were prepared and added separately to the corresponding solutions of compound **2**. The completion of the reaction was monitored by thin-layer chromatography (TLC). The solvent was then evaporated, and the residue was washed with diethyl ether to remove any unreacted components, yielding the target cationic Gemini surfactants (**3a–c**). Lastly, the products' melting points are lower than 100 °C, and they were vacuum dried at 40 °C.

2.2.3.1 N,N′-(((Oxybis(ethane-2,1-diyl))bis(oxy))bis(2-oxoethane-2,1-diyl))bis(3-dodecanamido-N,N-dimethylpropan-1-aminium) chloride (GSE-12). Yellowish white semisolid; yield = 89%. FT-IR (ATR) ν/cm^{-1}; 1197 (νC–O, ether), 1654 (νC=O amide), 1734 (νC=O ester), 2849–2917 (νCH aliphatic fatty chain), 3330–3351 (νNH stretching). ^{1}H NMR (500 MHz, DMSO-d_6) δ; 8.06 (t, J = 5.7 Hz, 2H), 4.61 (t, J = 5.5 Hz, 4H), 4.46 (s, 4H), 3.47–3.43 (m, 4H), 3.16 (s, 12H), 3.07–2.98 (m, 4H), 2.01 (t, J = 7.4 Hz, 4H), 1.82–1.73 (m, 4H), 1.47–1.38 (m, 4H), 1.24–1.12 (m, 32H), 0.80 (t, J = 6.9 Hz, 6H). ^{13}C NMR (101 MHz, DMSO-d_6) δ; 170.46, 165.81, 65.54, 62.47, 60.50, 50.75, 41.92, 41.02, 37.69, 31.39, 30.97, 28.84, 28.72, 28.50, 28.09, 27.48, 24.91, 22.64, 21.95, 20.65, 14.19.

2.2.3.2 N,N′-(((Oxybis(ethane-2,1-diyl))bis(oxy))bis(2-oxoethane-2,1-diyl))bis(N,N-dimethyl-3-tetradecanamidopropan-1-aminium) chloride (GSE-14). Pale brown viscous solid; yield = 90%. FT-IR (ATR) ν/cm^{-1}; 1021 (νC–O, ether), 1640 (νC=O amide), 1734 (νC=O ester), 2845–2927 (νCH aliphatic fatty chain), 3336–3354 (νNH stretching). ^{1}H NMR (500 MHz, DMSO-d_6) δ; 8.05 (s, 2H), 4.63 (s, 4H), 4.44 (s, 4H), 3.70 (s, 4H), 3.15 (s, 7H), 3.11 (s, 4H), 3.07–2.98 (m, 5H), 2.02 (t, J = 7.5 Hz, 4H), 1.77 (dd, J = 10.5, 6.0 Hz, 4H), 1.47–1.35 (m, 4H), 1.18 (s, 40H), 0.80 (t, J = 6.9 Hz, 6H). ^{13}C NMR (101 MHz, DMSO-d_6) δ; 171.71, 164.85, 65.77, 62.27, 60.67, 54.09, 50.99, 41.92, 31.30, 29.05, 29.02, 29.00, 28.95, 28.72, 28.62, 27.81, 25.22, 22.47, 22.10, 20.96, 13.94.

2.2.3.3 N,N′-(((Oxybis(ethane-2,1-diyl))bis(oxy))bis(2-oxoethane-2,1-diyl))bis(N,N-dimethyl-3-palmitamidopropan-1-aminium) chloride (GSE-16). Pale brown viscous solid; yield = 90%. FT-IR (ATR) ν/cm^{-1}; 1020 (νC–O, ether), 1652 (νC=O amide), 1733 (νC=O ester), 2841–2923 (νCH aliphatic fatty chain), 3325–3352 (νNH stretching). ^{1}H NMR (500 MHz, DMSO-d_6) δ; 8.06 (t, J = 5.7 Hz, 2H), 4.61 (t, J = 5.5 Hz, 4H), 4.46 (s, 4H), 3.71 (s, 4H), 3.17 (d, J = 12.7 Hz, 12H), 3.03 (dd, J = 12.3, 6.3 Hz, 4H), 2.01 (t, J = 7.5 Hz, 4H), 1.82–1.71 (m, 4H), 1.46–1.38 (m, 4H), 1.18 (s, 52H), 0.80 (t, J = 6.9 Hz, 6H). ^{13}C NMR (101 MHz, DMSO-d_6) δ; 174.06, 167.46, 65.91, 65.59, 62.48, 60.82, 51.26, 41.62, 40.63, 33.40, 31.39, 29.11, 29.03, 28.99, 28.90, 28.80, 28.67, 28.04, 25.28, 24.84, 23.48, 22.18, 14.01.

2.3 Critical micelle concentration (CMC) measurements

Using pure water and a platinum ring, the surface tension values at 298 K were measured using the K6 processor Tensiometer (KRÜSS Company, Germany). To reach equilibrium, the cationic Gemini surfactant solutions were maintained at 298 K for 20 hours. Before each measurement, the platinum ring was cleaned by repeatedly rinsing it with pure water to remove any surface impurities. Three readings were then made for each sample to demonstrate repeatability and get an average result.[32] Additionally, as reported in our previous study, the electrical conductivity (K) of the prepared cationic surfactant solutions at 298 K was measured using an electrical conductivity meter (Type AD3000; EC/TDS and temperature meter).[32]

2.4 Test of corrosion inhibition

2.4.1 Electrochemical study. A concentrated 37% (w/w) stock solution of hydrochloric acid ACS reagent, acquired from Sigma-Aldrich, was diluted to create the 3 M hydrochloric acid used in the investigation. Slow bubble rates were used in the study to simulate corrosion conditions found in the industry. By attaching an air-filled syringe to a 2 mm tube immersed in the electrolyte, setting the syringe pump to a low, steady flow rate, and adjusting the flow rate until the observed detachment happens every two seconds, air bubbles (with 0.45 mL min^{-1} flow rate) were introduced into the electrochemical cell. The goal of this method is to mimic the precise interactions between gas bubbles and liquids that might cause corrosion in industrial environments, like those that occur during chemical processing or water treatment. An essential component of many corrosion processes is the presence of oxygen, or air. Because of the electrochemical reactions involving oxygen, the tests increase the likelihood of corrosion by adding air to the system. In order to mimic the gradual, prolonged exposure to corrosive chemicals, modest-low bubble rate is essential.

The low-carbon steel (AISI 1026) specimens were cylindrical in shape and had a diameter of 0.25 cm. Their composition (in wt%) was as follows: 0.283 carbon, 0.266 silicon, 0.481 manganese, 0.017 phosphorus, 0.041 sulfur, and 0.13 chromium, with iron (Fe) making up the remaining fraction.

Before putting into the polarization cell, the specimen was cleaned with double-distilled water, degreased with acetone, and polished with silicon carbide paper (1000/600 grit). Before beginning the polarization scan, the specimen was given time (an hour) to reach a steady open circuit voltage. The reference electrode for the measurement of equilibrium potential is the saturated calomel electrode (SCE). The BioLogic SP-150 potentiostat connected to a computer running EC-Lab® software was used to run and analyse both the polarization curves and the Nyquist plots. A scan rate of 1 mV s^{-1} was used to produce linear polarization measurements, which ranged from −1.1 V to −0.2 V (with respect to OCP). To determine the corrosion current density (i_{corr}), corrosion potential (E_{corr}), anodic slope (β_a), and cathodic slope (β_c), we used the conventional Tafel extrapolation method. The electrochemical impedance diagrams were carried out using an excitation signal of 10 mV and a frequency range of 100 kHz to 10 mHz. Both electrochemical procedures were carried out three times following an hour of immersion to ensure reliability.

The inhibition efficiency (η) was determined using the equations:[33–35]

$$\eta_{PDP} = \frac{i_{corr.Blank} - i_{corr.GSE}}{i_{corr.Blank}} \times 100 \quad (1)$$

$$\eta_{EIS} = \frac{R_{ct.GSE} - R_{ct.Blank}}{R_{ct.GSE}} \times 100 \quad (2)$$

where, $i_{corr.Blank}$ and $i_{corr.GSE}$ are the corrosion current densities, while $R_{ct.Blank}$ and $R_{ct.GSE}$ are the charge transfer resistance, all for blank and GSE-inhibited solutions, respectively.

2.4.2 Surface analysis, film stability and thermal resistance test. After being submerged for 1, 24, 36, 48, and 72 h in 100 mL of aerated 3 M HCl solution, AISI 1026 coupons were taken out, cleaned with distilled water and acetone, dried, and weighed to determine the average weight loss $\Delta W = W_i - W_f$ (mg); the experiment is repeated twice with and without 0.1 mmol L^{-1} GSE. The corrosion rate of AISI 1026 and inhibition efficieny of GSE inhibitor were determined using the following equations:[36]

$$CR_W = \frac{\Delta W}{At} \quad (3)$$

$$\eta_W = \frac{CR_{W,f} - CR_{W,GSE}}{CR_{W,f}} \quad (4)$$

where t is the exposure period, A is the coupon's surface area (15 cm^2), and $CR_{W,f}$ and $CR_{W,GSE}$ are the corrosion rates of AISI 1026 in mg cm^{-2} h^{-1} with and without GSE surfactant, respectively.

The surface of the carbon steel specimens was analysed using SEM-EDX (JSM-IT700HR/LA) at an acceleration voltage of 15 kV used to scan the carbon steel specimens after 1 h exposure time in room temperature as well as after heating the medium to 50 °C. Also, the adsorbed film was skimmed from the carbon steel surface and introduced to FTIR analysis using a Thermos Nicolet iS10 FTIR spectrophotometer.

3 Quantum calculations and simulations

3.1 DFT calculations

The molecular structures of inhibitors GSE-12, GSE-14, and GSE-16 were initially built and visualized using GaussView 6.0 molecular modelling software.[37] Geometry optimizations were performed for both the unprotonated (neutral) and the most stable protonated forms of each molecule to locate ground state minimum energy configurations. All calculations were carried out with the Gaussian 09, Revision D.01 program suite employing density functional theory (DFT) with the B3LYP hybrid functional and the 6-31G(d,p) basis set.[38] To account for solvent effects representative of acidic aqueous environments, the conductor-like polarizable continuum model (CPCM) was applied throughout all optimizations and property evaluations.[39] Frequency calculations confirmed the absence of imaginary frequencies, validating that true minima had been achieved. For each optimized structure, frontier molecular orbital properties including the energies of the highest occupied molecular orbital (E_{HOMO}) and lowest unoccupied molecular orbital (E_{LUMO}), the LUMO–HOMO energy gap (ΔE), and number of electrons transferred (ΔN) was determined by the following equation:

$$\Delta N = \frac{\phi - \chi_{inh}}{2\eta_{inh}} \quad (5)$$

where ϕ equal to 4.82 eV for Fe(110).[40] Additionally, electrostatic potential (ESP) maps and the spatial distributions of HOMO and LUMO were generated to visualize the charge distribution and reactive sites across the molecular surfaces. This comprehensive computational protocol was applied consistently to all protonation states of GSE-12, GSE-14, and GSE-16 to enable reliable comparisons of their electronic structures and adsorption behaviours.

3.2 Monte Carlo simulations

Monte Carlo simulations were conducted using the Adsorption Locator module within Materials Studio 2016 (Accelrys) to investigate the adsorption behaviour of inhibitors GSE-12, GSE-14, and GSE-16 on the Fe(110) surface. The Fe(110) substrate was constructed by cleaving bulk iron along the (110) crystallographic plane, resulting in a four-layer slab with lateral dimensions of 15 × 15 Å and a 40 Å vacuum region normal to the surface to avoid artificial interactions between periodic images. Each inhibitor was treated as a single molecule in the simulation cell, accompanied by 150 explicit water molecules, 5 hydronium ions (H_3O^+), and 5 chloride ions to mimic the acidic aqueous environment realistically. The Condensed-phase Optimized Molecular Potentials for Atomistic Simulation Studies (COMPASS) force field was employed for all energy evaluations and structural optimizations.[41] The Ewald

summation was used to evaluate electrostatic forces and van der Waals forces were treated by an atom-based method. Prior to simulation, each inhibitor molecule was geometry optimized using COMPASS to obtain its minimum energy conformation. The lowest energy inhibitor–Fe(110) configurations were selected, and relevant descriptors including adsorption energy was recorded. The adsorption energy was computed as the difference in total energy between the optimized adsorbate–substrate complex and the sum of the isolated optimized inhibitor, clean Fe(110) slab, and solvent components. This systematic approach enabled a quantitative comparison of the adsorption strength and structural preferences of GSE-12, GSE-14, and GSE-16 in conditions closely resembling the corrosive environment.

4 Results and discussion

4.1 Chemistry

In this work, dodecanoic, tetradecanoic, and hexadecenoic acids were used to design a novel series of ionic liquid-based cationic Gemini surfactants (**3a–c**), which were subsequently investigated as corrosion inhibitors. As found in Scheme 1, the FA (dodecanoic, tetradecanoic, and hexadecenoic) was treated with *N*,*N*-dimethylpropane-1,3-diamine in the presence toluene as a solvent and PTSA as a catalyst to produce *N*-(3-(dimethylamino)propyl)alkanamides (**1a–c**). The synthesized compounds were characterized by FTIR, which showed the appearance of the amide carbonyl bands at 1635 and 1652 cm^{-1} and the disappearance of the carboxylic acid carbonyl band (Fig. S2). Concurrently, diethylene glycol, chloroacetic acid, and *p*-toluenesulfonic acid (PTSA) as a catalyst were mixed in dry toluene and refluxed to produce oxybis(ethane-2,1-diyl)bis(2-chloroacetate) (**2**). The FTIR showed the appearance of ester group at 1738 cm^{-1} and the disappearance of OH groups of alcohol. Interestingly, the ^{1}H NMR spectrum showed the appearance of three sets of 4H ($2 \times CH_2$) signals with significant deshielding, while the ^{13}C NMR spectrum displayed a new peak at 173.05 ppm corresponding to the ester carbonyl, along with three peaks for different CH_2 groups (Fig. S1). Finally, the *N*-(3-(dimethylamino)propyl)alkanamides (**1a–c**) was quaternized with oxybis(ethane-2,1-diyl)bis(2-chloroacetate) (**2**) in acetonitrile to generate the targeted ionic liquids based cationic Gemini surfactants (**3a–c**).

For the final products (**3a–c**), the characteristic peaks observed in the spectra can be interpreted as follows. In the FT-IR spectrum given in Fig. S3–S5, the peak band at 3300–3336 cm^{-1} refers to the amide N–H bond (stretching). The peaks at 2918–2927 cm^{-1} and 2841–2854 cm^{-1} refers to the aliphatic C–H (stretching), the peak at 1734 and 1733 cm^{-1} indicates the C=O (stretching) in carbonyl on the ester bond, the peak band at 1654–1640 cm^{-1} refers to the C=O (stretching) in carbonyl on the amide bond, and the peak band at 1197–1020 cm^{-1} belongs to the C–O stretching on the ester bond.[42]

As shown in Fig. S3–S5, the ^{1}H NMR spectra display a peak at approximately 8.05 ppm, corresponding to the N–H proton of the amide functional group. In addition, there are peaks at 4.44–4.63 ppm that correspond to the hydrogens of the CH_2 group attached to the positively charged nitrogen atom and the hydrogens of the CH_2 group bound to the oxygen atom of the ester group, and at 3.7 ppm, hydrogens that originate from the CH_2 group adjacent to the ether (C–O) group are detected. Lastly, peaks at 0.78–2.02 ppm that relate to the hydrogen of the fatty chain were observed.

Through the ^{13}C NMR spectrum of the as-prepared compounds shown in Fig. S3–S5, the peaks referring to the carbonyl carbon of amide are at 170 and 171 ppm; the peak belonging to the carbonyl carbon of ester is at 164, 165 ppm; in addition to these, other characteristic carbon atoms peaks were appeared such as the peak of carbon of CH_2 adjacent to the oxygen of ether group at 65 ppm; the peak of CH_2 carbon adjacent to the oxygen of ester group at 60–62 ppm; the peak band of CH_2 carbons of fatty chain at 20–30 ppm, and the CH_3 carbon peak band at the very end of the lengthy chain at 13.94 ppm.

4.2 The CMC measurements

Surface tension and electrical conductivity were measured at various surfactant concentrations to determine the CMC values of the cationic Gemini surfactants at 25 °C, and the results of CMC values are displayed in Fig. 1A and B. The CMC value for each surfactant was calculated by plotting the obtained values as a function of concentration (ln Conc.) of the surfactant solutions, and the results are displayed in Fig. 1A. Furthermore, as illustrated in Fig. 1C, it was noted that the CMC values obtained using both methods were extremely comparable, falling within 1.2–3.6 mmol L^{-1}; *via* surface tension, the CMC of 3.6 ± 0.15, 1.6 ± 0.12, and 1.3 ± 0.15 mmol L^{-1} (Fig. 1A) and *via* electrical conductivity, the CMC of 1.5 ± 0.16, 1.3 ± 0.14, and 1.2 ± 0.12 mmol L^{-1} (Fig. 1B) were acquired for the as-prepared surfactants GSE-12, GSE-14, and GSE-16, respectively. Interestingly, the lengthening of carbon chain length affects CMC values; the surfactant with the shortest chain length (GSE-12) had the greatest CMC value, while the one with the longest chain length (GSE-16) had the lowest. Furthermore, the CMC values obtained in this study are lower than those reported for common surfactants such as DHPB (4.47 mM),[43] which has a similar fatty chain length. In contrast, the ionic liquid-based Gemini cationic surfactants, having two lipophilic tails, exhibit even lower CMC values. Interestingly, our study's CMC values are lower than those of previous Gemini surfactants, including GSBO, GSBD, and GSBH.[44,45]

The effectiveness of corrosion inhibition is fundamentally tied to the adsorption capacity of surfactant molecules, which mirrors their ability to aggregate into micelles. This process can be broken down based on the Critical Micelle Concentration (CMC). Below CMC, as the concentration of the surfactant increases, molecules preferentially migrate to the interface. During this stage, the metal surface acts as the primary site for surfactant accumulation, leading to a steady reduction in surface tension and the initial formation of a protective barrier. At the CMC, this point serves as a critical threshold. Near this concentration, the metal surface typically achieves saturation, becoming covered by a stable monolayer of surfactant

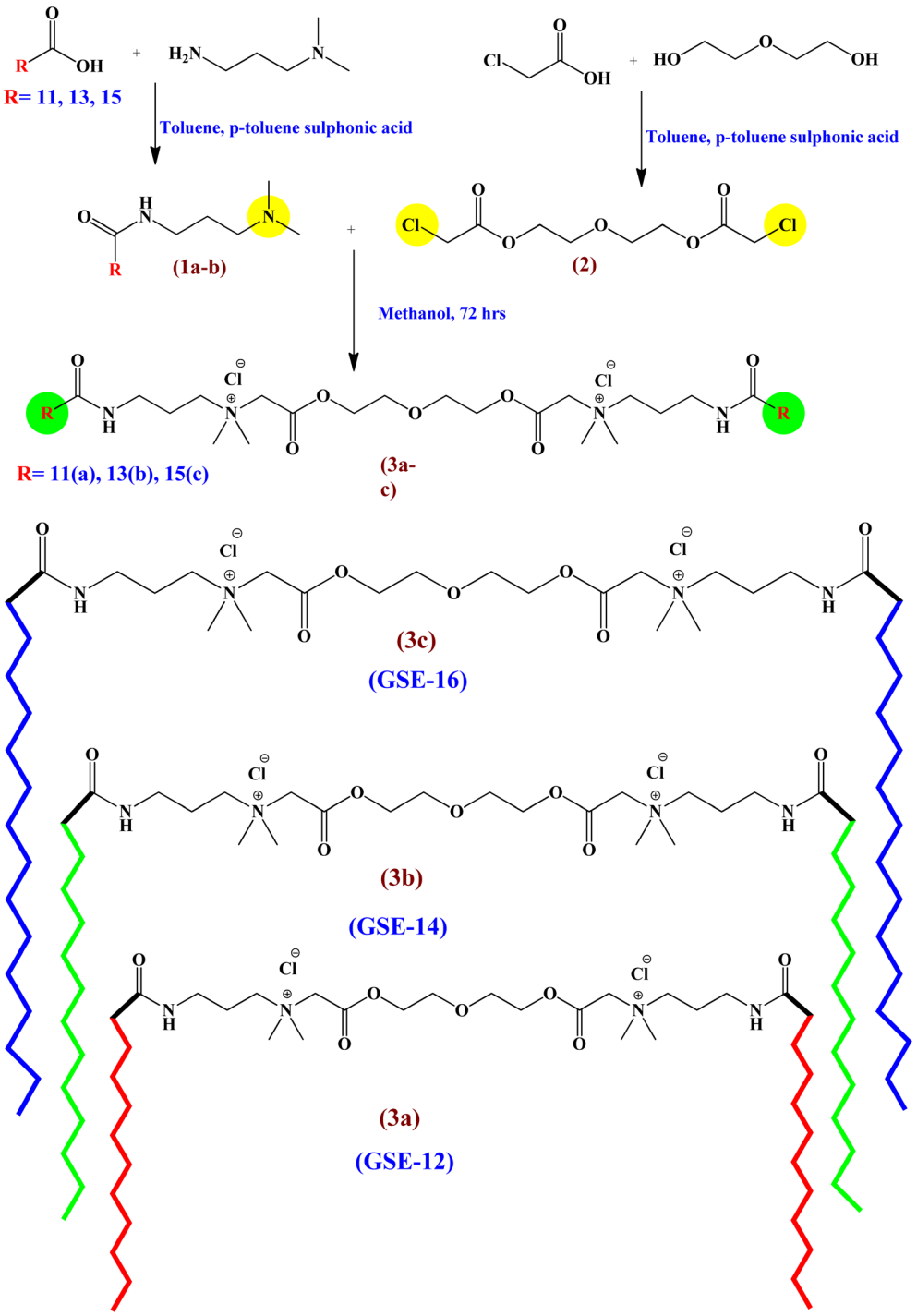

Scheme 1 Synthesis of the target ionic liquids-based cationic Gemini surfactants (3a–c).

molecules. This usually represents the peak of inhibition efficiency. Above CMC, once the CMC is exceeded, additional surfactant molecules no longer contribute significantly to surface coverage. Instead, they begin to aggregate within the bulk solution to form micelles or may start building secondary layers (multilayers) on the surface. The CMC is a vital diagnostic tool for engineering corrosion protection. By using it as a benchmark, operators can optimize inhibitor dosing, ensuring that exactly enough chemical is applied to reach maximum surface saturation. This precision prevents the wasteful over-use of chemicals (where molecules would simply form micelles) while ensuring the highest possible protection for the metal infrastructure.[46,47]

4.3 OCP curves

The open-circuit potential (OCP), also known as the zero-current potential (ZCP), is the maximum potential difference between two electrodes that can be measured without applying

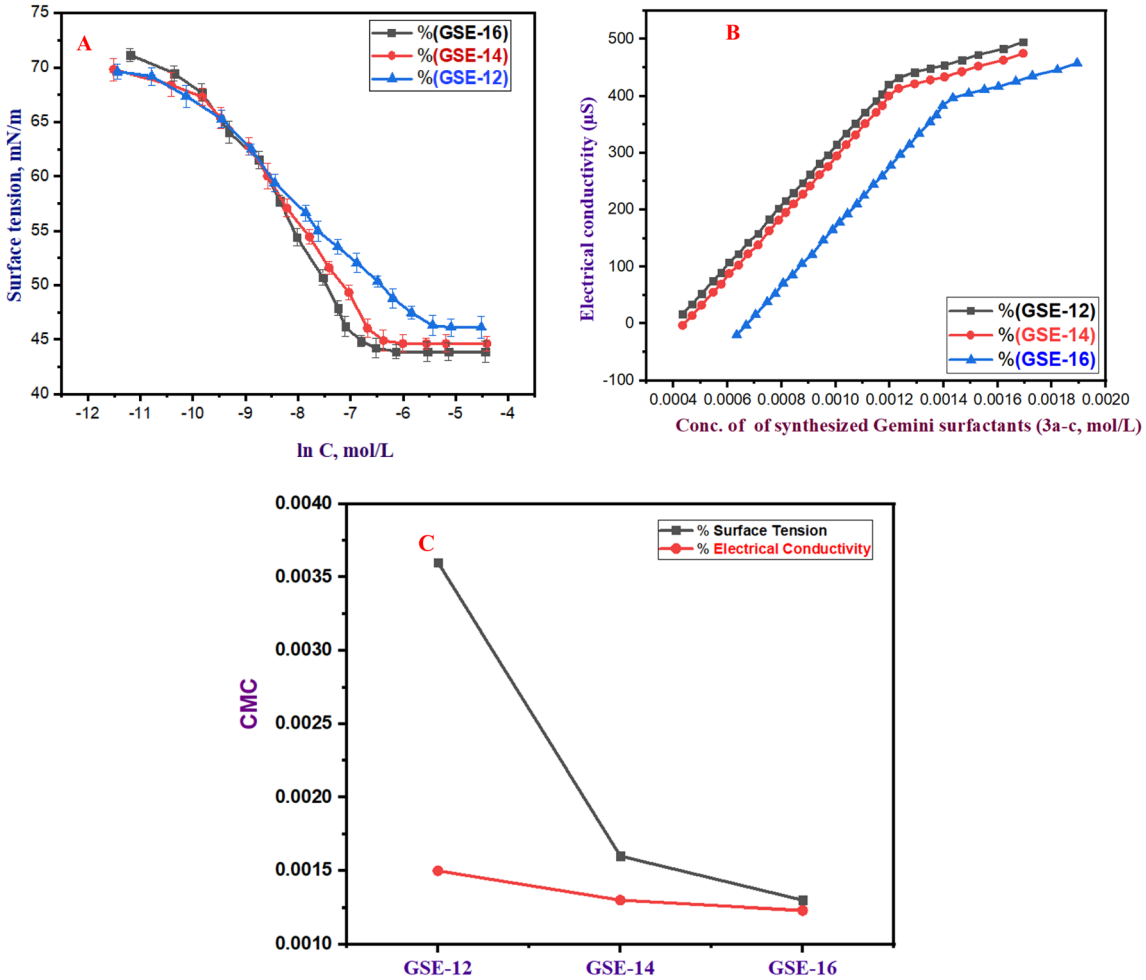

Fig. 1 Variation of (A) surface tension and (B) specific conductivity *vs.* the concentration of ionic liquids-based Gemini cationic surfactants at 25 °C, and (C) represents the synthesized surfactants (GSE-12, GSE-14, and GSE-16) with the CMC values.

an external current. Since there is no current flowing through, measuring the OCP is non-destructive. It is commonly employed to ascertain the resting potential of the system. One method that could shed some light on the stability of electrochemical processes is OCP. This implies that if the OCP stays constant for a long time, the system might be stable or at least sufficiently stable thermodynamically.[48] Monitoring corrosion processes is aided by monitoring the OCP or corrosion potential. Since the system would much rather absorb electrons than lose them, larger positive corrosion potentials appear advantageous and increase the likelihood of reduction processes. The sample is oxidizing and accumulating negative charges if the corrosion potential is decreasing. The OCP potential is used to conduct the EIS test. In the polarization test, the anodic and cathodic reactions polarize with respect to the OCP potential. For stability over time, OCP gives the ideal time to conduct electrochemical techniques. As a result, OCP can be measured over time prior to conducting electrochemical techniques, allowing for the estimation of the necessary minimum test time.[49]

Fig. 2 shows the open circuit potential (OCP) curves for the carbon steel immersed in a 3 M HCl acid solution at 25 °C.

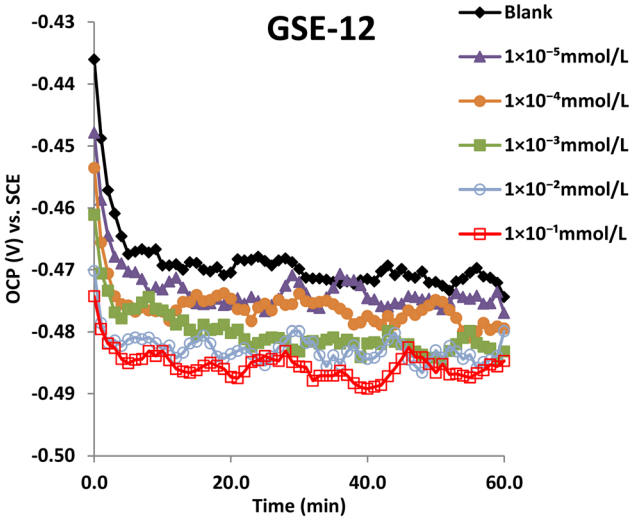

Fig. 2 Open circuit potential during the first hour of AISI 1026 immersion in aerated 3 M HCl solution.

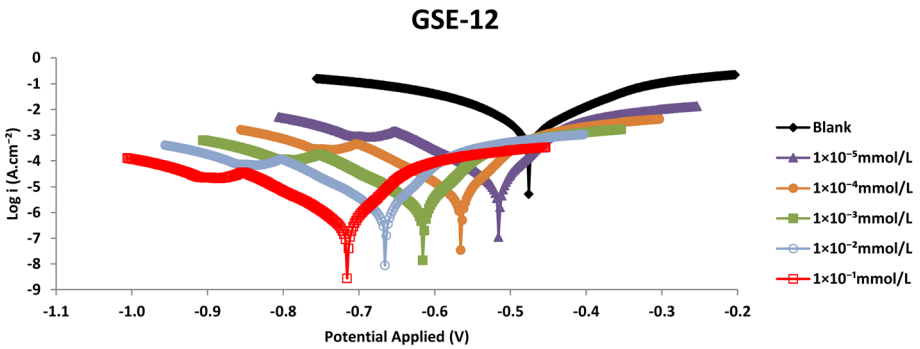

Fig. 3 Potentiodynamic polarization curves of AISI 1026 in aerated 3 M HCl solution free of and with presence of different GSE-12 concentrations.

These curves show the evolution of the potential as a function of immersion time, in the absence and presence of GSE-12 inhibitor at different concentrations. Generally, the potentials range between −0.34 V and −0.49 V, suggesting that the working electrode is corroding over time, Fig. 2 and S6. The adsorption of GFE-12 inhibitor onto the steel surface is responsible for the initial potential's progressive shift towards increasingly negative values in each instance until stabilizing. Regardless of the concentration, the curves display comparable shapes. Additionally, there were very slight changes in potential after 30 minutes of immersion. This indicates that equilibrium is reached after this period, allowing electrochemical measurements to be conducted under stable conditions. It appears that inhibitors cause the potential to shift toward negative values. This does not necessarily mean that the working electrode is subject to increased corrosion. But at least, it may suggest that inhibitors have the ability to stimulate the electrode to expel electrons for inhibitor adsorption onto the cathodic sites of the metal surface, as will be approved later.[50]

4.4 Potentio-dynamic polarization (PDP) curves

The potentiodynamic curves in the absence and presence of GSE at different concentrations are shown in Fig. 3 and S7. Generally, the Tafelian regime demonstrates that a pure activation mechanism controls the metal/solution interaction.[51] Although these inhibitors cause little change in the anodic slope (154 mV dec^{-1} to 162 mV dec^{-1}), they significantly affect the cathodic slope (−163 mV dec^{-1} to −218 mV dec^{-1}), resulting in a negative shift of the corrosion potential from −476 mV to −716 mV, which clearly indicates cathodic inhibition, as also suggested by the OCP measurements. It appears that the ammonium groups of GSE surfactants are attracted to the negatively charged sites on the carbon steel surface, leading to changes in the cathodic reactions at the carbon steel/solution interface. These GSE surfactants can also adsorb at the interface with their hydrophobic tails oriented away from the highly ionic medium, thereby covering the metal surface (both anodic and cathodic sites) and inhibiting corrosion. This reduces both anodic and cathodic reactions, resulting in effective mixed-type corrosion inhibition with cathodic predominance.[52,53]

Table 1 Potentiodynamic polarization parameters of AISI 1026 in aerated 3 M HCl solution free of and with presence of different GSE concentrations

Solution	Conc. (mmol L^{-1})	β_c (mV dec^{-1})	β_a (mV dec^{-1})	E_{corr} (mV)	i_{corr}[a] (μA cm^{-2})	η	θ
Blank	—	−163	154	−476	16.45 ± 0.412	—	—
GSE-12	0.00001	−201	154	−516	1.01 ± 0.035	93.86	0.94
	0.0001	−211	160	−566	0.87 ± 0.020	94.71	0.95
	0.001	−210	158	−616	0.83 ± 0.027	94.95	0.95
	0.01	−202	162	−666	0.82 ± 0.021	95.02	0.95
	0.1	−218	161	−716	0.81 ± 0.028	95.08	0.95
GSE-14	0.00001	−204	162	−513	1.37 ± 0.039	91.67	0.92
	0.0001	−205	162	−533	1.3 ± 0.035	92.10	0.92
	0.001	−214	159	−553	1.07 ± 0.027	93.50	0.93
	0.01	−208	158	−573	1.06 ± 0.025	93.56	0.94
	0.1	−217	160	−593	1.01 ± 0.024	93.86	0.94
GSE-16	0.00001	−205	160	−514	2.59 ± 0.062	84.26	0.84
	0.0001	−209	161	−522	2.22 ± 0.063	86.50	0.87
	0.001	−206	160	−532	1.93 ± 0.056	88.27	0.88
	0.01	−214	162	−552	1.7 ± 0.059	89.67	0.90
	0.1	−203	162	−582	1.51 ± 0.048	90.82	0.91

[a] The relative standard deviation for i_{corr} values is ±3%.

Analysis of Table 1 shows that GSE-12 inhibitor has the highest inhibitory efficiency, while GSE-16 has the lowest η value. The corrosion inhibition performance of the Gemini surfactants appears to be due to the inverse relationship between the surface-active characteristics and the extremely high hydrophobicity. A protective barrier with moderate hydrophobicity can form on the metal surface; however, excessive hydrophobicity may cause issues such as poor solubility, reduced adsorption, and the formation of hydrophobic layers that trap corrosive species.[54–56]

4.5 Impedance diagrams

Electrochemical Impedance Spectroscopy (EIS) is a useful method for investigating metal corrosion and how to prevent corrosion. EIS analyzes the system's impedance response to an applied alternating current (AC) signal to offer information on the metal–electrolyte interface and the performance of corrosion inhibitors. The impedance data, Nyquist and Bode plots, can be analyzed to determine parameters like charge transfer resistance (R_{ct}) and double-layer capacitance (C_{dl}), which are essential for evaluating inhibitor performance and corrosion mechanisms.

The Nyquist diagram of carbon steel in the inhibitor-free aerated 3 M HCl solution shows a single-capacitive loop and one charge transfer mechanism during the oxidation of carbon steel. The Nyquist diagram, however, displays a double-capacitive loop when GSE inhibitors are present, suggesting that two charge transfer processes occurred during the oxidation of carbon steel in the aerated 3 M hydrochloric acid solution and GSE adsorption, Fig. 4 and S8. The Bode plot exhibits two-time constants in the presence of GSE inhibitors, whereas only a single time constant is observed in the inhibitor-free aerated 3 M HCl solution.[57] With the help of EC-Lab® software, the appropriate equivalent circuits were chosen to fit the EIS data. Maximum iterations were set to 100. Charge transfer resistance (R_{ct}), solution resistance (R_S), and double-layer capacitor (C_{dl}) are all included for the blank solution. The suggested equivalent circuit for the Nyquist loops in presence of GSE inhibitors was a R_S-2RC-type equivalent circuit; the solution resistance (R_S) in series with a 2RC model fitted well. The first RC circuit consists of the charge transfer resistance (R_{ct}), which represents the resistance to carbon steel dissolution, in parallel with the double-layer capacitance (C_{dl}) formed at the carbon steel/solution interface. The second RC circuit is formed by the development of a barrier layer with a film resistance (R_f) that prevents charge transfer during the electrochemical process and a capacitance (C_f) made with deposits serving as dielectrics. The PDP results, which show decreases in the cathodic current densities of carbon steel at specific potentials, support the formation of protective deposits.[58] The size of the Nyquist loops, and consequently the film and charge transfer resistances, increases with GSE concentration, confirming that

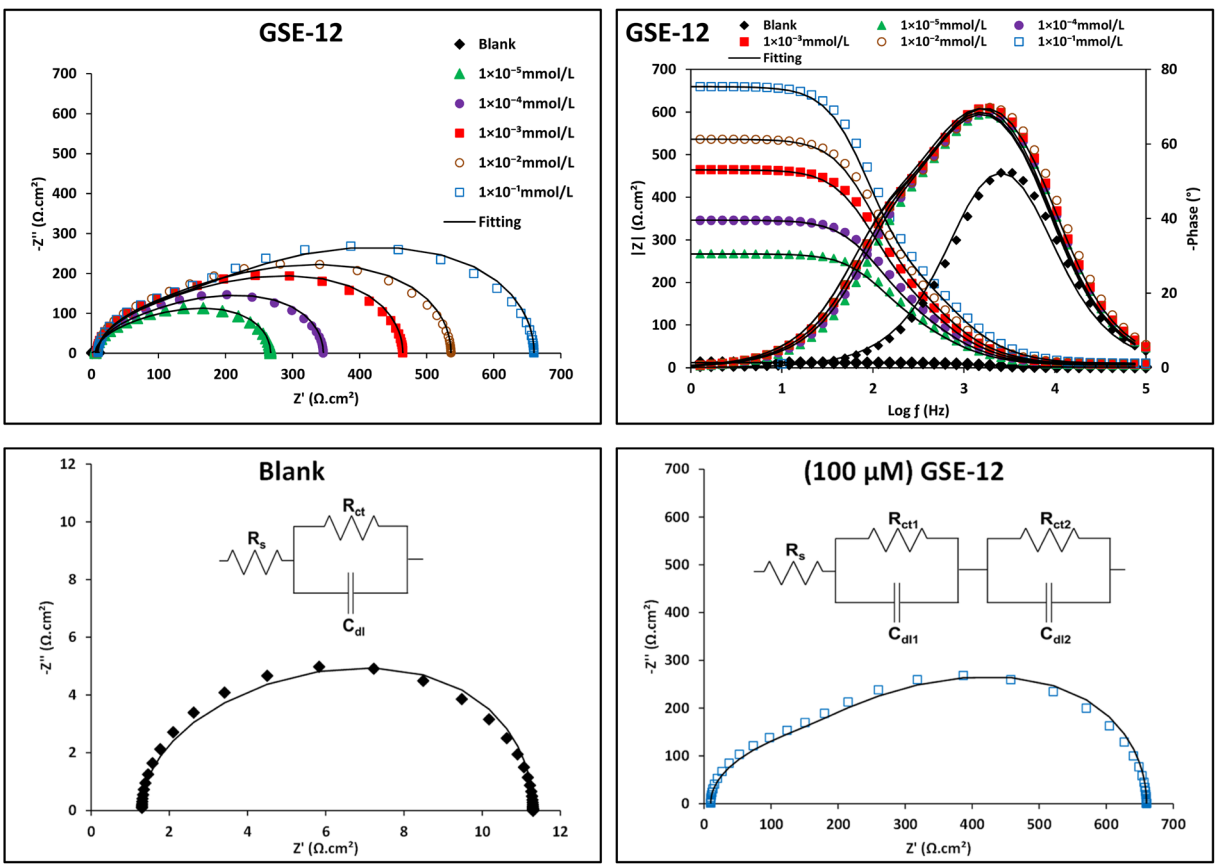

Fig. 4 EIS diagrams of AISI 1026 in aerated 3 M HCl solution free of- and with presence of different GSE-12 concentrations.

Table 2 EIS data of AISI 1026 in aerated 3 M HCl solution free of and with presence of different GSE concentrations ($\chi^2 \approx 10^{-5}$)

Solution	Conc. (mmol L^{-1})	R_S (Ω)	N_{dl}	Y_{0dl} (μS s^N)	C_{dl} (μF)	R_{ct} (Ω)	N_f	Y_{0f} (μS s^N)	C_f (μF)	R_f (Ω)	η	θ
Blank	—	1.30	0.86	100	29	10.0	0.84	—	—	—	—	—
GSE-12	0.00001	6.11	0.86	42	12	200.8	0.84	31	8	60.2	95.02	0.95
	0.0001	7.25	0.85	36	10	260.4	0.88	25	9	78.1	96.16	0.96
	0.001	8.46	0.87	31	10	350.7	0.87	20	6	105.2	97.15	0.97
	0.01	9.22	0.85	27	7	405.4	0.80	16	3	121.6	97.53	0.98
	0.1	10.00	0.86	25	7	500.0	0.84	10	2	150.0	98.00	0.98
GSE-14	0.00001	5.10	0.89	51	19	100.9	0.90	40	17	30.3	90.09	0.90
	0.0001	6.49	0.84	43	10	150.6	0.86	32	9	45.2	93.36	0.93
	0.001	7.44	0.80	38	6	220.4	0.82	27	5	66.1	95.46	0.95
	0.01	8.96	0.85	31	8	305.7	0.87	20	6	91.7	96.73	0.97
	0.1	9.11	0.85	29	8	400.3	0.88	18	6	120.1	97.50	0.98
GSE-16	0.00001	4.50	0.81	62	12	85.1	0.85	51	14	25.5	88.25	0.88
	0.0001	5.48	0.86	51	15	92.4	0.83	40	9	27.7	89.18	0.89
	0.001	6.01	0.85	44	12	100.6	0.85	33	9	30.2	90.06	0.90
	0.01	7.12	0.86	38	11	200.4	0.83	27	6	60.1	95.01	0.95
	0.1	8.42	0.80	31	5	300.7	0.85	20	5	90.2	96.67	0.97

the increasing number of GSE molecules enhances inhibition against corrosive acidic agents.

The impedance parameters' values obtained by fitting the electrical equivalent circuits to impedance spectra are summarized in Table 2. Given that the chi-square values (χ^2) fall around 10^{-5}, the simulation and the experimental findings appear to be consistent. Table 2 illustrates that both R_{ct} and R_f rise with increasing GSE concentrations. This is most likely due to GSE molecules sticking to the carbon steel surface and creating an inhibitory barrier layer in the interface between the carbon steel and the corrosive electrolyte, which stops or slows down the electrochemical corrosion reaction and raises η.[59]

Estimation of the true double-layer (C_{dl}) capacitance values is done through the coming equation:[60]

$$C_{dl} = Y_{0dl}\omega^{n-1} = Y_{0dl}(2\pi f_{max})^{n-1} \quad (6)$$

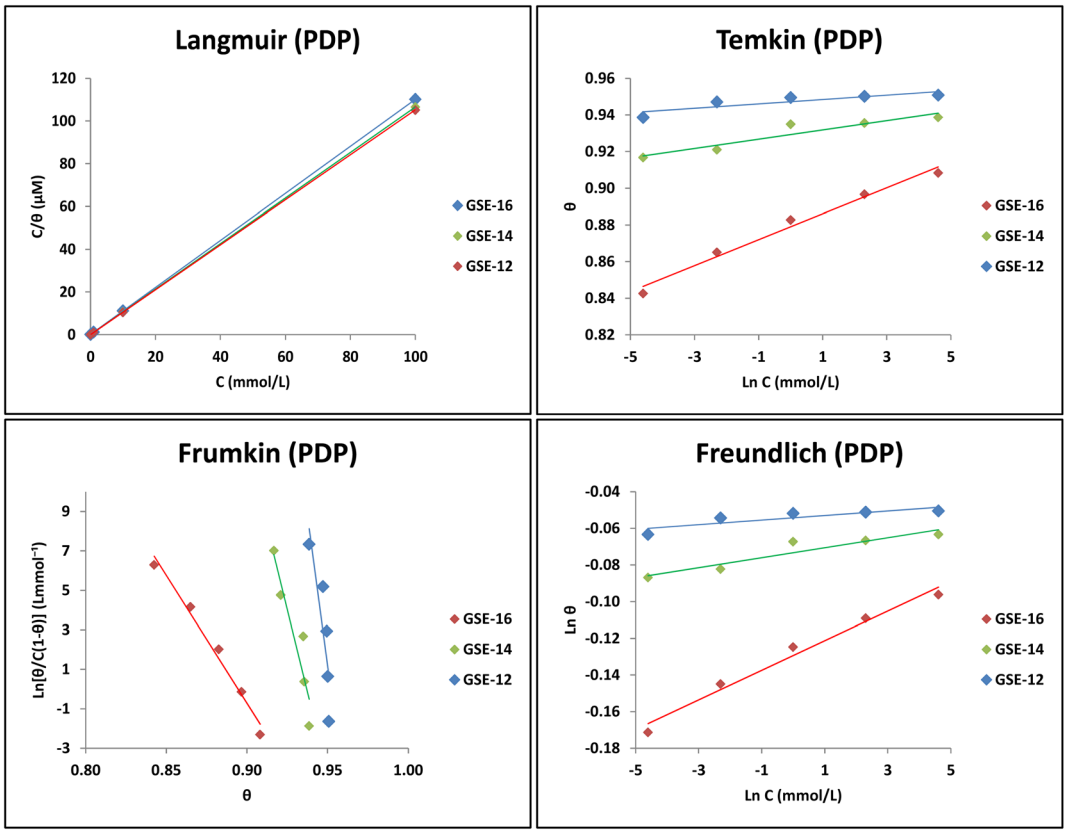

Fig. 5 Several adsorption isotherms describing the adsorption behaviour of GSE inhibitors on AISI 1026 in aerated 3 M HCl solution.

Table 3 Adsorption constant and adsorption free energy of the adsorption of GSE inhibitors on AISI 1026 in aerated 3 M HCl solution

Surfactant	Technique	Temkin R^2	Frumkin R^2	Freundlich R^2	Langmuir R^2	K_{ads} (μM^{-1})	ΔG°_{ads} (kJ mol^{-1})
GSE-12	PDP	0.74	0.73	0.74	1.00	480.44	−59.49
	EIS	0.95	0.94	0.95	1.00	69.23	−54.69
GSE-14	PDP	0.88	0.87	0.88	1.00	101.51	−55.64
	EIS	0.93	0.92	0.93	1.00	37.78	−53.19
GSE-16	PDP	0.98	0.98	0.98	1.00	23.02	−51.96
	EIS	0.91	0.87	0.91	1.00	15.35	−50.96

where Y_{0dl} is a parameter for a constant phase element (CPE) in place of a true double layer capacitor (C_{dl}), n is CPE exponent, f_{max} is the frequency at which the imaginary component of the impedance is maximal.

The inhibition effect was further confirmed by the Bode diagrams, where the impedance modulus ($|Z|$) increases with increasing GSE concentration. Moreover, it is evident that the phase angle values surpass those of the blank and get closer to the ideal capacitor when GSE inhibitor is present. This suggests that the adsorbed GSE molecules at the interface enhance the barrier properties of the protective layer. At the carbon steel/electrolyte interface, these GSE molecules may take the place of water molecules, increase the surface coverage and successfully protect the carbon steel from the corrosive acidic surroundings. As a result, the double-layer thickness grew and the C_{dl} decreased.

The inhibition efficiency η, charge transfer resistance R_{ct} and film resistance R_f trends of the three GSE inhibitors have the order GSE-12 > GSE-14 > GSE-16, as concluded from PDP results.

4.6 Adsorption isotherms

To better understand the corrosion inhibition process and to select effective inhibitors, it is important to examine the adsorption behaviour of these substances through studying their adsorption isotherms which provide information on the extent of adsorption, the strength of the inhibitor–metal interaction, and the mode of adsorption (physisorption or chemisorption).

Numerous adsorption isotherm types, such as Langmuir, Temkin, Frumkin, and Freundlich, have been investigated to comprehend the adsorption mechanism of GSE molecules on the carbon steel surface in the aerated 3 M HCl solution, Fig. 5 and S9. With the help of the determined surface coverage θ from both PDP and EIS data, these adsorption isotherms are given by the next equations:[61]

$$\text{Langmuir}: \quad \frac{C_{GSE}}{\theta} = C_{GSE} + \frac{1}{K_{ads}} \tag{7}$$

$$\text{Temkin}: a\theta = \ln K_{ads} + \ln C_{GSE} \tag{8}$$

$$\text{Frumkin}: \quad \ln\left\{\frac{\theta}{C_{GSE}(1-\theta)}\right\} = \ln K_{ads} + g\theta \tag{9}$$

$$\text{Freundlich}: \ln\theta = \ln K_{ads} + n \ln C_{GSE} \tag{10}$$

The Langmuir isotherm has the best linearity (with correlation coefficient nearly equal to one) among the isotherms examined above, as seen by Table 3 analysis of the experimental data. It appears that the adsorption process is partially reversible, and the GSE molecules form a monolayer on the carbon steel surface without causing interference. By analysing the relationship between the GSE concentration and the surface coverage θ (or inhibition efficiency η divided by 100), it is possible to gain insights into the adsorption mechanism and determine thermodynamic parameters of adsorption.

In order to understand the mechanism of adsorption, the standard free energy of adsorption ΔG°_{ads} is calculated:[62]

$$\Delta G^{\circ}_{ads} = -RT \ln(C_{Water} \ K_{ads}) \tag{11}$$

where C_{Water} is the number of moles of water in one litre which is taken the value 55.5.

The ΔG°_{ads} values obtained from both PDP and EIS measurements were consistent and reliable. The ΔG°_{ads} values obtained are between −59.49 kJ mol^{-1} and −50.96 kJ mol^{-1}, typically explained by the GSE molecules' physical and chemical adsorption behaviour on the carbon steel surface. Indeed, GSE molecules spontaneously adsorb onto the carbon steel surface as ΔG values are negative.

4.7 Surface analysis (SEM-EDX and FTIR studies)

A very flexible method for obtaining high-resolution pictures and comprehensive surface information of samples is scanning electron microscopy. A specimen's surface is scanned by the concentrated electron beam, producing images with resolutions ranging from less than one nanometres to several nanometres.[63]

SEM-EDX analysis was performed on samples immersed in aerated 3 M HCl solution, both in the absence and presence of 0.1 mmol L^{-1} GSE-12 inhibitor, at 25 °C and after heating to 50 °C for one hour.

SEM images (Fig. 6) show that the carbon steel surface is severely damaged in the absence of GSE-12 inhibitor, particularly after heating at 50 °C for one hour. In contrast, in the presence of 0.1 mmol L^{-1} GSE-12 inhibitor, the surface remains smoother and less deteriorated at both 25 and 50 °C. The most likely cause of this is the GSE-12 inhibitor molecules adhering to the carbon steel's surface and creating a barrier between it and the corrosive acidic medium.[64]

The EDX spectra show that the oxygen content significantly decreases in the presence of GSE (from 8.74% at 25 °C and 18.63% at 50 °C to 4.32% at 25 °C and 5.35% at 50 °C), while the

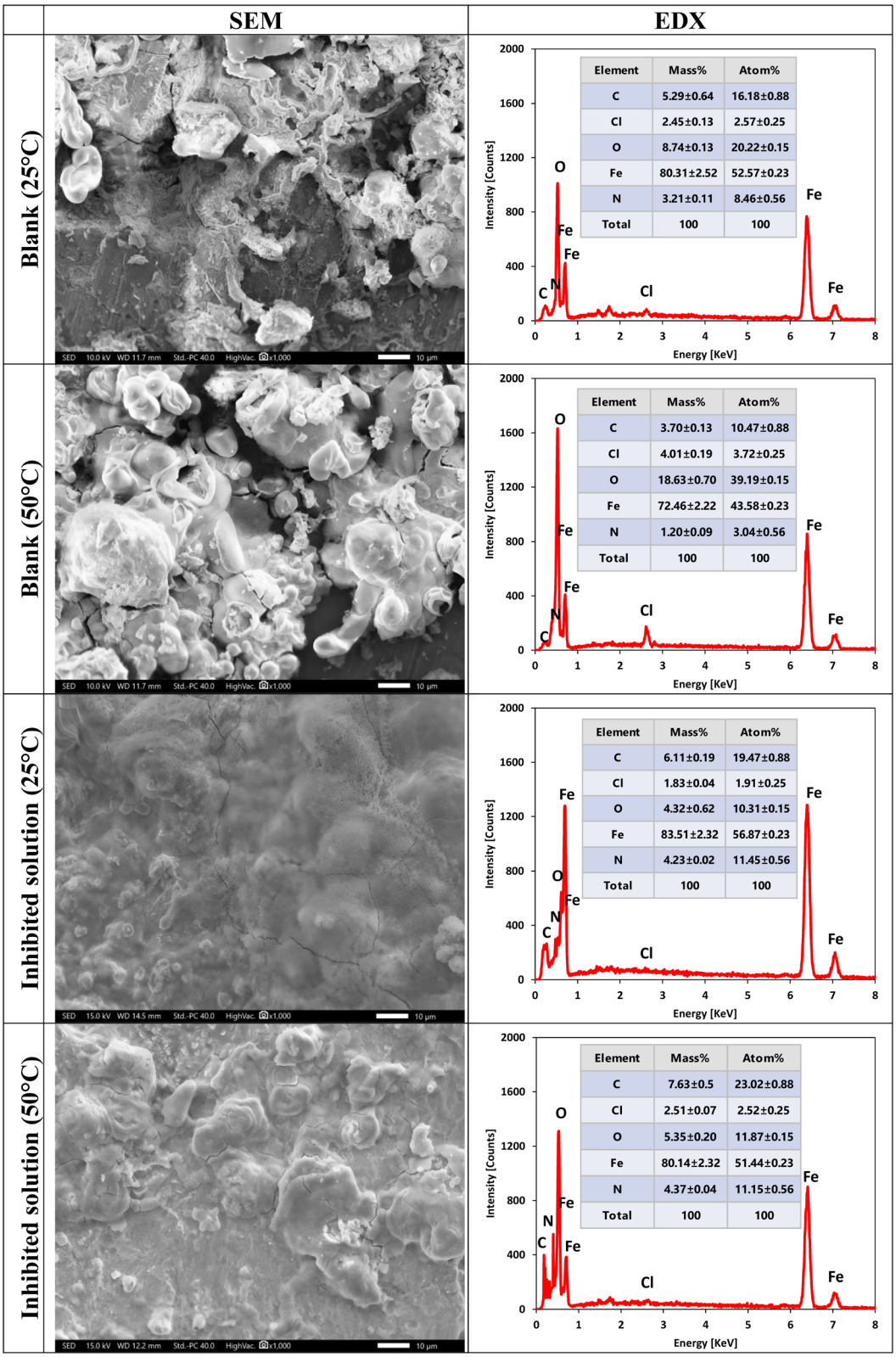

Fig. 6 SEM-EDX for AISI 1026 after one hour immersion in aerated 3 M HCl solution at 25 °C and after heating to 50 °C, free of and in presence of GSE-12.

carbon content increases slightly (from 5.29% at 25 °C and 3.70% at 50 °C to 6.11% at 25 °C and 7.63% at 50 °C). Also, a significant diminution of percentage of Cl ions was noted. Moreover, the nitrogen amount is noted to be higher in presence of GSE-12 (4.23% at 25 °C and 4.37% at 50 °C) than in its absence (3.21% at 25 °C and 1.20% at 50 °C). Finally, the iron

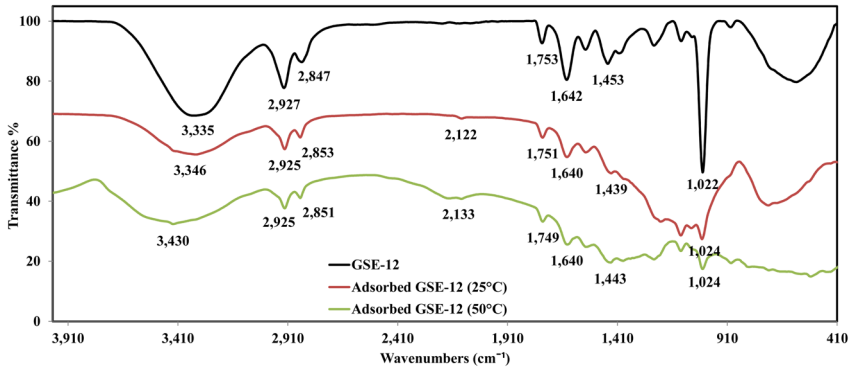

Fig. 7 FTIR of GSE-12 before and after immersion of AISI 1026 in aerated 3 M HCl solution for one hour at 25 °C and after heating to 50 °C.

amount is increased from 80.31% at 25 °C and 72.46% at 50 °C to 83.51 at 25 °C and 80.14 at 50 °C. These findings show that, in the absence of GSE-12 inhibitor, the surface is more covered with corrosion products, such as iron oxides and iron chlorides. The chemisorption of GSE molecules on the carbon steel surface may be the cause of the increased carbon content when GSE inhibitor is present. This is consistent with the above electrochemical techniques' findings on the GSE inhibitors' notable inhibitory efficacy.[65]

Adsorbed corrosion inhibitors on metal surfaces can be examined using Fourier Transform Infrared Spectroscopy (FTIR), which offers details on how the inhibitor interacts with the metal and forms a protective layer. Whether the inhibitor interacts with the metal *via* chemisorption or is retained on the surface through weak physical adsorption, FTIR analysis can help identify the inhibition mechanism. It is possible to ascertain if the inhibitor is attached to the metal and the type of binding by comparing the FTIR spectra of the adsorbed layer and the pure inhibitor. The presence of particular functional groups in the adsorbed layer can reveal information about how the inhibitor and metal interact. For instance, various peaks in the FTIR spectrum can suggest that the inhibitor is attaching itself to the metal by means of specific functional groups, such as carboxyl's, amines, or others. By monitoring changes in the spectrum of the adsorbed layer, FTIR can indirectly assess the effectiveness of inhibition, even though its primary purpose is to provide qualitative information on adsorption and inhibitor–metal interactions. For instance, the inhibitor may effectively prevent corrosion if the FTIR spectra indicate the formation of a clear protective layer on the metal surface.[66]

In Fig. 7, the peaks for the extracted film from the surface of the carbon steel after one hour immersion in the aerated 3 M HCl solution with 0.1 mmol L^{-1} GSE-12 inhibitor are: 3346, 2853–2925, 1751, 1640 and 1024 cm^{-1} at room temperature, and 3430, 2851–2925, 1749, 1640 and 1024 cm^{-1} after heating to 50 °C. These peaks are close to the NH stretching, the aliphatic fatty chain, the ester, the amide and ether of the GSE-12 before immersion, suggesting the adsorption action and GSE withstanding at elevated temperatures up to 50 °C as approved electrochemically.

Changes in the surrounding chemical environment, such as hydrogen bonding or other intermolecular interactions like adsorption onto the metal, may cause shifts in FTIR spectrum. The skimmed film from the carbon steel surface after one hour immersion showed new bands at 2122 cm^{-1} at 25 °C and 2133 cm^{-1} at 50 °C. This is likely due to the carbonyl (C=O) stretching vibration of the GSE-12 surfactant adsorbed on the metal surface, suggesting that the carbonyl group interacts with Fe in both zero and higher oxidation states.[67,68] A higher wavenumber shift (a blue shift) is observed at higher temperature (50 °C) generally indicates an increase in bond strength, a stronger interaction with the metal at higher temperatures. Also, if a molecule forms a hydrogen bond, the bond strength may change, and the corresponding peak may shift to a higher wavenumber.

In general, it is noted that some peaks are shifted while others are somewhat displaced. This could be a sign of several modifications to the molecule or its surroundings as a result of hydrogen bonding, interaction with the carbon steel, and the existence of corrosion products.[69]

Table 4 Thermodynamic parameters of AISI 1026 in aerated 3 M HCl solution free of and in presence of 0.1 mmol L^{-1} GSE-12 inhibitor after one hour immersion and at different temperatures (the limits of the relative standard uncertainties for CR are ± 6%)

Solution	T (K)	CR (mg cm^{-2} h^{-1})	η	E_a (kJ mol^{-1})	ΔH^* (kJ mol^{-1})	ΔS^* (J mol^{-1} K^{-1})
Blank	298	1.865	—	27.04	24.46	−188.30
	313	2.542				
	323	5.777				
0.1 mmol L^{-1} GSE-12	298	0.050	97.32	34.25	31.68	−134.29
	313	0.067	97.36			
	323	0.121	97.91			

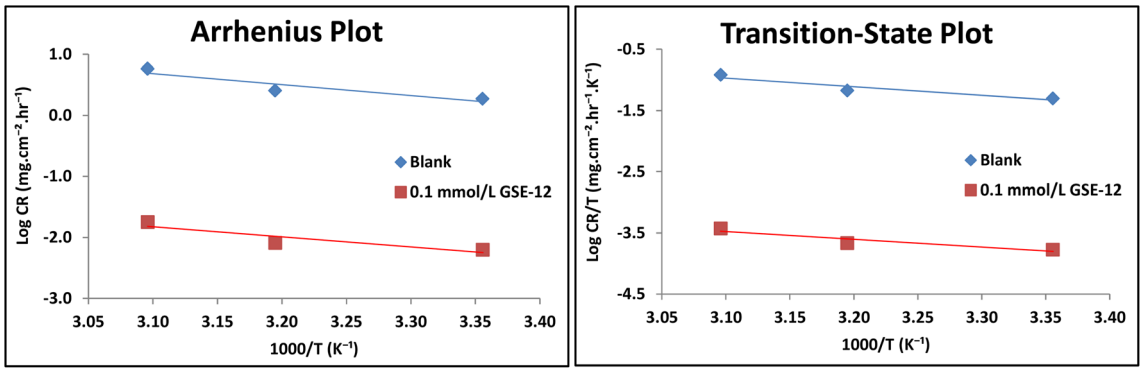

Fig. 8 Arrhenius and transition-state plots of AISI 1026 in aerated 3 M HCl solution free of and in presence of 0.1 mmol L^{-1} GSE-12 inhibitor.

Table 5 Corrosion rate of AISI 1026 in mg cm^{-2} h^{-1} and inhibition efficiency η of 100 μM GSE-12 with time in aerated 3 M HCl solution

	1 h		24 h		36 h		72 h	
Solution	CR_W	η	CR_W	η	CR_W	η	CR_W	η
Blank	1.865	—	3.011	—	5.054	—	7.677	—
0.1 mmol L^{-1} GSE-12	0.050	97.32	0.263	91.27	0.56	88.96	0.888	88.43

4.8 Kinetics parameters

By examining how temperature affects corrosion rates, and the energetics of the corrosion process, Arrhenius and transition state theory are utilized to explain how corrosion inhibitor's function.

The Arrhenius equation describes how reaction rates change with temperature plotting ln(corrosion rate) *versus* $1/T$ establishes a relationship between temperature and corrosion rate, where A is the frequency factor, R is the ideal gas constant, and T is the temperature. The slope is equal to $-E_a/R$, allowing for the determination of the activation energy E_a.[70]

$$\ln \mathrm{CR} = \ln A - \frac{E_a}{RT} \tag{12}$$

A more thorough understanding of the reaction mechanism is offered by transition state theory, sometimes referred to as activated complex theory. It focuses on the transition state or the activated complex, which is the reaction's greatest energy state. Transition state plots involve plotting ln(corrosion rate/T) against $1/T$. The slope and intercept of this plot are related to thermodynamic parameters like enthalpy of activation (ΔH^*) and entropy of activation (ΔS^*).[71]

$$\ln\left(\frac{\mathrm{CR_W}}{T}\right) = \left[\ln\left(\frac{R}{N_A h}\right) + \frac{\Delta S^*}{R}\right] - \frac{\Delta H^*}{RT} \tag{13}$$

The process of corrosion inhibition can be better understood, and the inhibitor's effectiveness can be optimized by examining the changes in these parameters (E_a, ΔH^* and ΔS^*) brought about by the presence of the inhibitor.

The GSE inhibitors begin to precipitate above 50 °C in the aerated 3 M HCl solution. Therefore, we ranged our temperatures from 25 to 50 °C to study their inhibition action on carbon

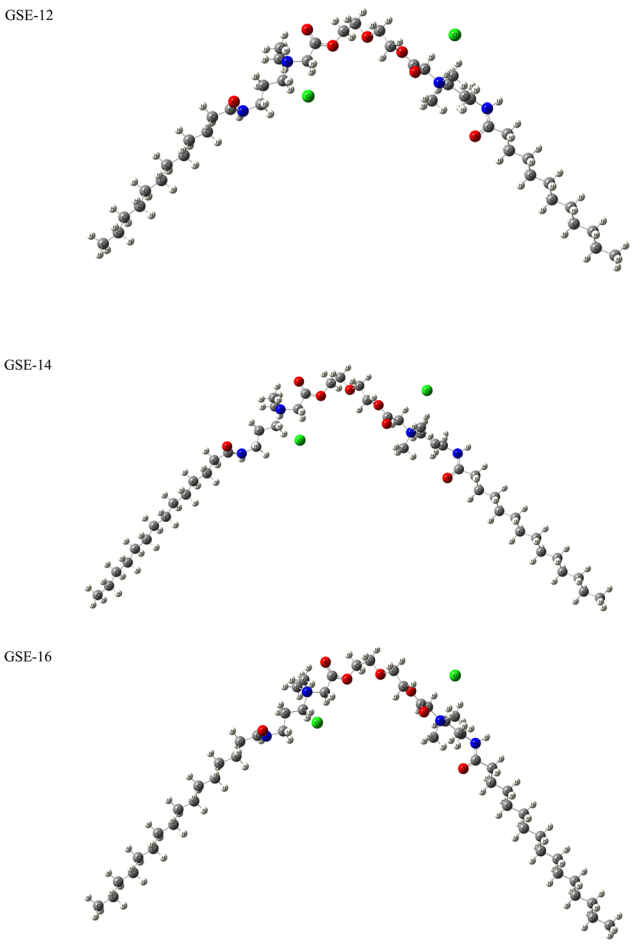

Fig. 9 Optimized structures of GSE-12, GSE-14 and GSE-16 inhibitors.

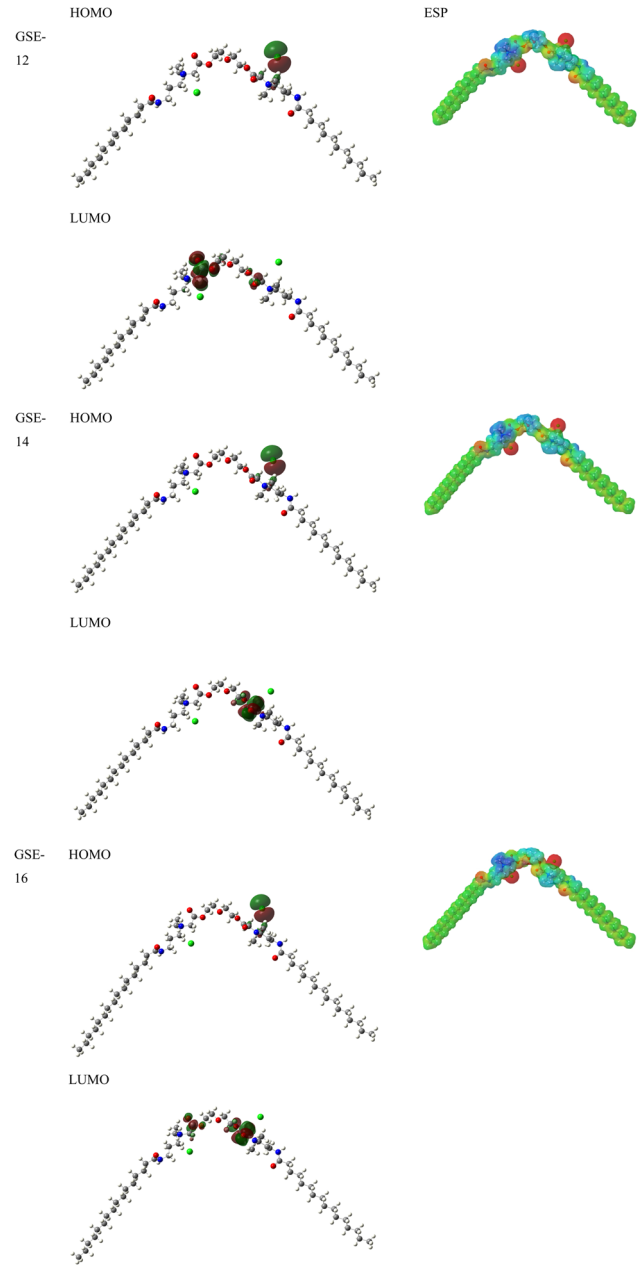

Fig. 10 Frontier orbitals and electrostatic potential maps of GSE-12, GSE-14 and GSE-16 inhibitors.

steel in the present test. Weight loss was measured before and after one hour of immersion at 25, 40, and 50 °C, and used to determinate the corrosion rate (mg cm^{-2} h^{-1}) and the inhibition efficiency (η).

Table 4 shows the calculated inhibition efficiencies η and the activation parameters E_a, ΔH^* and ΔS^*. In general, the GSE inhibitor increases the activation energy (E_a) and the enthalpy of activation (ΔH^*), as the adsorbed GSE molecules on the carbon steel surface create a higher energy barrier that slows down the corrosion reaction. The entropy ΔS^* is increased in presence of GSE inhibitor, indicating a change in the structure of the activated complex (Fig. 8).[72]

Our conclusion is that GSE inhibitors can adsorb onto the metal surface, creating a barrier that hinders the movement of ions or electrons involved in the corrosion process. This adsorption is physico–chemical in nature, as the inhibition efficiency (η) increases with rising temperature, most likely due to electrostatic interactions and/or electron transfer with the metal's d-orbitals (Table 4).

4.9 Testing the durability of GSE inhibitor over time

A reliable method to evaluate the GSE durability as a corrosion inhibitor and its film development on a metal surface over time is to compare the weight loss of the tested alloy with and without the surfactant in a corrosive medium. Table 5 demonstrates how the corrosion rate of AISI 1026 specimens in the aerated 3 M HCl solution increases drastically over time and how the addition of GSE dramatically lowers the corrosion rate throughout a range of timeframes, up to three days. Therefore, it makes sense to conclude that GSE surfactants are effective corrosion inhibitors at the tested conditions. For up to three days, by creating hydrophobic films that prevent the corrosive liquid, GSE molecules can adsorb onto metal surfaces and protect them. Even though it decreased with time, η showed acceptable levels after three days of exposure.

4.10 DFT study

DFT calculations provide atomic-scale electronic-structure insights into molecule–metal interactions and, when combined with Monte Carlo adsorption sampling and experimental validation, underpin our mechanistic understanding of corrosion inhibition. In our study, we first optimized the geometries of GSE-12, GSE-14 and GSE-16 as seen in Fig. 9 and then visualized their frontier orbitals (Fig. 10), before extracting the key electronic descriptors summarized in Table 6. Here, the E_{HOMO} value pinpoints those regions most prone to donate electron density into the vacant d-orbitals of Fe(110), while E_{LUMO} highlights the sites most capable of accepting back-donated charge. A higher E_{HOMO} thus signals superior electron-donor strength, and a lower E_{LUMO} indicates enhanced electron-acceptor ability.[73,74] In both their unprotonated and

Table 6 Quantum parameters for GSE-12, GSE-14 and GSE-16 inhibitors

	Unprotonated form				Protonated form			
Compound	E_{HOMO} (eV)	E_{LUMO} (eV)	ΔE (eV)	ΔN (e)	E_{HOMO} (eV)	E_{LUMO} (eV)	ΔE (eV)	ΔN (e)
GSE-12	−6.339	−0.441	5.898	0.242	−6.363	−0.660	5.703	0.229
GSE-14	−6.337	−0.451	5.886	0.242	−6.364	−0.786	5.578	0.223
GSE-16	−6.337	−0.438	5.899	0.243	−6.363	−0.662	5.701	0.229

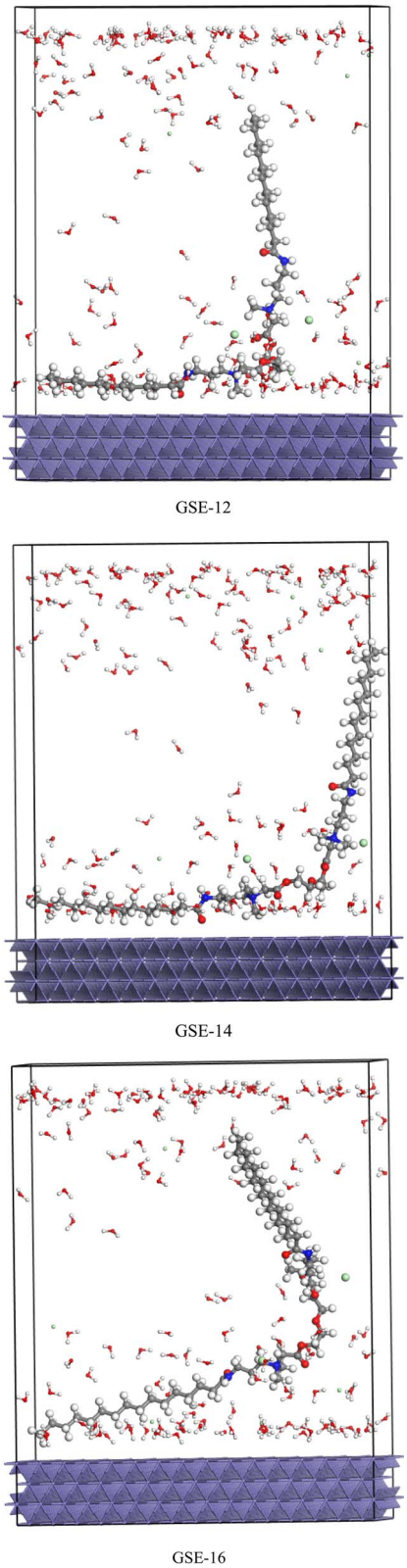

Fig. 11 Adsorption views of GSE-12, GSE-14 and GSE-16 inhibitors on Fe(110) surface.

protonated forms. In the unprotonated state, all three inhibitors exhibit very similar E_{HOMO} (≈ -6.34 eV) and E_{LUMO} (≈ -0.44 to -0.45 eV) values, yielding ΔE values of roughly 5.89–5.90 eV and fractional electron transfer values $\Delta N \approx 0.242$–0.243 e. On first glance, GSE-14's marginally lower gap (5.886 eV) might hint at slightly higher reactivity, but when we examine the protonated forms, a clearer distinction emerges. Upon protonation, GSE-12's ΔE drops modestly from 5.898 to 5.703 eV, accompanied by only a slight decrease in ΔN from 0.242 to 0.229 e. In comparison, GSE-14 experiences a reduction in ΔE (to 5.578 eV) but also a more pronounced loss in ΔN (down to 0.223 e), and GSE-16 mirrors GSE-12's ΔE change (to 5.701 eV) but with the same slightly lower ΔN (0.229 e). These shifts tell us that, although GSE-14 becomes energetically "softer" when protonated, it simultaneously sacrifices electron donor capacity more than GSE-12. In contrast, GSE-12 retains the highest ΔN under acidic conditions, meaning it preserves the greatest ability to donate electron density into the vacated Fe d-orbitals even after protonation. With its relatively balanced ΔE, low enough to allow efficient back-donation but not so low as to make the inhibitor overly polarized and less stable, GSE-12 achieves an optimal donor–acceptor balance. This superior electronic profile, evident in both neutral and protonated environments, underpins GSE-12's markedly stronger adsorption energy on Fe(110) and explains why it outperforms GSE-14 and GSE-16 in forming a cohesive, mixed type cathodic inhibition.

As seen in Fig. 10, the HOMO localization on the chloride counter ion indicates that the highest energy occupied electrons are concentrated on chloride, making it the most favorable electron-donating site for interaction with the vacant Fe d-orbitals. This unusual HOMO distribution suggests that the adsorbed chloride may act as a co-inhibitor by supplying electron density directly to the metal surface, reinforcing the protective film formed by the organic molecule. Meanwhile, the LUMO being localized on the carboxylate moiety indicates that this site is the primary acceptor of electron density back-donation from filled Fe d-states. This dual HOMO/LUMO partitioning Cl ion as the electron donor and carboxylate moiety as the electron acceptor supports a mixed physisorption–chemisorption mechanism.

Electrostatic potential (ESP) maps translate a molecule's three dimensional charge distribution into an intuitive colour code, blue for electron poor (positive) regions, red for electron rich (negative) regions, and green for areas of near neutral potential, thereby pinpointing where nucleophiles and electrophiles are most likely to attack.[75,76] As seen in Fig. 10, the most intense blue patches appear on nitrogen atom and certain hydrogen atoms, indicating these sites carry a relative positive potential and will attract incoming electron-rich species (nucleophiles). Conversely, the red zones cluster around the

Table 7 Adsorption of GSE-12, GSE-14 and GSE-16 inhibitors on Fe(110) surface

System	Adsorption energy (kcal mol^{-1})
GSE-12 + Fe(110)	−681.95
GSE-14 + Fe(110)	−617.04
GSE-16 + Fe(110)	−597.16

carbonyl and adjacent oxygen atoms in the linker moiety and chloride ion, marking them as electron dense centres that can readily donate charge to electrophilic partners.

4.11 MC simulations

Fig. 11 provides a comparative visualization of how the three inhibitors orient themselves upon adsorption onto the Fe(110) surface. GSE-12 and GSE-14 adopts a partially planar arrangement, where significant portions of the molecular framework remain close to parallel with the Fe(110) plane, but some parts particularly the terminal substituents extend upward into a more vertical orientation. This mixed binding mode indicates that while the aromatic core retains effective π–d overlap, the electron-withdrawing substituent introduces steric repulsion or torsional strain that limits full planar contact. As a result, GSE-14 achieves moderately strong adsorption, but with fewer simultaneous interaction points compared to GSE-12. The GSE-16 displays a distinctly tilted adsorption conformation, where one segment of the molecule inclines at a notable angle relative to the iron surface, and another portion stands nearly upright. Adsorption energies (E_{ads}) as seen in Table 7, computed on a periodic Fe(110) slab quantify the thermodynamic driving force for inhibitor binding. GSE-12 binds with an exceptionally negative E_{ads} of −681.95 kcal mol^{-1}, reflecting a highly exergonic adsorption. GSE-14 (−617.04 kcal mol^{-1}) and GSE-16 (−597.16 kcal mol^{-1}) also adsorb favorably but lose ∼64 and ∼85 kcal mol^{-1}, respectively, owing to their less extensive HOMO overlap and steric tilting induced by substituents. This roughly 10–12% difference in adsorption energy corresponds to a substantially lower equilibrium surface coverage for GSE-14 and GSE-16. Experimentally, polarization studies classify all three as mixed-type inhibitors with predominantly cathodic control, but GSE-12 consistently shows the greatest suppression of cathodic current density.

5 Conclusion

GSE surfactants have the ability to adsorb onto the carbon steel in aerated 3 M HCl solution at different temperatures and extended periods of exposure, protecting the metal from corrosion with inhibition efficiency of 98.00% for GSE-12, 97.50% for GSE-14 and 96.67% for GSE-16 after 1 h. The very high hydrophobicity in a high ionic solution is not preferred. Langmuir adsorption isotherm is the fitted model for these surfactants. These surfactants can adsorb spontaneously with physical attraction and chemical interaction due to the relatively high Gibbs free energy ΔG°_{ads} values which reached −59.49 kJ mol^{-1} for GSE-12. The thermodynamic parameters, the activation energy E_a, the activation enthalpy ΔH^* and the entropy ΔS^* increase with GSE presence in the corrosion system. Reliability was observed in the experimental results. The computational findings correlate well with experimental evidence showing GSE-12 as the most effective mixed-type inhibitor with dominant cathodic control of corrosion processes, due to the consistency between the surface activity and the moderate hydrophobicity of the inhibitor.

Conflicts of interest

There are no conflicts to declare.

Data availability

The data supporting the findings of this study are available upon request. Additional datasets generated and analyzed during the current study are included in the article and its supplementary information (SI). Further information is available from the corresponding author at a reasonable request. Supplementary information: spectroscopic analysis, OCP, PDP, and EIS diagrams curves of carbon steel. See DOI: https://doi.org/10.1039/d5ra08814c.

Acknowledgements

This research has been funded by Scientific Research Deanship at University of Ha'il – Saudi Arabia through project number (RG-25007).

References

1 L.-G. Qiu, A.-J. Xie and Y.-H. Shen, A novel triazole-based cationic Gemini surfactant: synthesis and effect on corrosion inhibition of carbon steel in hydrochloric acid, *Mater. Chem. Phys.*, 2005, **91**, 269–273.
2 S. A. Jafar, A. A. Aabid and J. I. Humadi, Corrosion behavior of carbon steel in 1 M, 2 M, and 3 M HCl solutions, *Mater. Today: Proc.*, 2022, **57**, 412–417.
3 D. Dwivedi, K. Lepková and T. Becker, Carbon steel corrosion: a review of key surface properties and characterization methods, *RSC Adv.*, 2017, **7**, 4580–4610.
4 P. D. Desai, C. B. Pawar, M. S. Avhad and A. P. More, Corrosion inhibitors for carbon steel: A review, *Vietnam J. Chem.*, 2023, **61**, 15–42.
5 F. E.-T. Heakal and A. E. Elkholy, Gemini surfactants as corrosion inhibitors for carbon steel, *J. Mol. Liq.*, 2017, **230**, 395–407.
6 R. Aslam, M. Mobin, J. Aslam and H. Lgaz, Sugar based N, N′-didodecyl-N, N′ digluconamideethylenediamine Gemini surfactant as corrosion inhibitor for mild steel in 3.5% NaCl solution-effect of synergistic KI additive, *Sci. Rep.*, 2018, **8**, 3690.
7 M. Mobin and R. Aslam, Experimental and theoretical study on corrosion inhibition performance of environmentally benign non-ionic surfactants for mild steel in 3.5% NaCl solution, *Process Saf. Environ. Prot.*, 2018, **114**, 279–295.
8 M. Mobin, R. Aslam and J. Aslam, Non toxic biodegradable cationic Gemini surfactants as novel corrosion inhibitor for mild steel in hydrochloric acid medium and synergistic effect of sodium salicylate: Experimental and theoretical approach, *Mater. Chem. Phys.*, 2017, **191**, 151–167.
9 M. El Achouri, M. R. Infante, F. Izquierdo, S. Kertit, H. Gouttaya and B. Nciri, Synthesis of some cationic Gemini surfactants and their inhibitive effect on iron corrosion in hydrochloric acid medium, *Corros. Sci.*, 2001, **43**, 19–35.

10 M. Hegazy, A novel Schiff base-based cationic Gemini surfactants: synthesis and effect on corrosion inhibition of carbon steel in hydrochloric acid solution, *Corros. Sci.*, 2009, **51**, 2610–2618.
11 M. Abdallah, M. Hegazy, M. Alfakeer and H. Ahmed, Adsorption and inhibition performance of the novel cationic Gemini surfactant as a safe corrosion inhibitor for carbon steel in hydrochloric acid, *Green Chem. Lett. Rev.*, 2018, **11**, 457–468.
12 T. Mao, H. Huang, D. Liu, X. Shang, W. Wang and L. Wang, Novel cationic Gemini ester surfactant as an efficient and eco-friendly corrosion inhibitor for carbon steel in HCl solution, *J. Mol. Liq.*, 2021, **339**, 117174.
13 M. Mobin and S. Masroor, Cationic gemini surfactants as novel corrosion inhibitor for mild steel in 1M HCl, *Int. J. Electrochem. Sci.*, 2012, **7**, 6920–6940.
14 S. A. El-Maksoud, F. El-Dossoki, M. Abd-Elhamed and A. A. Farag, Some new synthesized gemini cationic surfactants as corrosion inhibitors for carbon steel in hydrochloric acid solution, *J. Bio Tribo Corros.*, 2023, **9**, 71.
15 M. Deyab, I. Z. Ibrahim, O. A. El-Shamy, K. A. Khalil, A. F. Awad, M. M. Alghamdi, A. A. El-Zahhar and M. A. Abo-Riya, Synthesis, surface activity, and corrosion inhibition capabilities of new non-ionic gemini surfactants, *Sci. Rep.*, 2024, **14**, 8040.
16 X. Wang, H. Yang and F. Wang, A cationic gemini-surfactant as effective inhibitor for mild steel in HCl solutions, *Corros. Sci.*, 2010, **52**, 1268–1276.
17 M. Mobin and S. Noori, Adsorption and corrosion inhibition behaviour of zwitterionic gemini surfactant for mild steel in 0.5 M HCl, *Tenside Surfactants Deterg.*, 2016, **53**, 357–367.
18 O. Kaczerewska, R. Leiva-Garcia, R. Akid, B. Brycki, I. Kowalczyk and T. Pospieszny, Effectiveness of O-bridged cationic gemini surfactants as corrosion inhibitors for stainless steel in 3 M HCl: Experimental and theoretical studies, *J. Mol. Liq.*, 2018, **249**, 1113–1124.
19 M. Pakiet, I. H. Kowalczyk, R. L. Garcia, R. Akid and B. E. Brycki, Influence of different counterions on gemini surfactants with polyamine platform as corrosion inhibitors for stainless steel AISI 304 in 3 M HCl, *J. Mol. Liq.*, 2018, **268**, 824–831.
20 M. Abdel-Aal and M. Morad, Inhibiting effects of some quinolines and organic phosphonium compounds on corrosion of mild steel in 3M HCl solution and their adsorption characteristics, *Br. Corros. J.*, 2001, **36**, 253–260.
21 P. K. Chattaraj and D. R. Roy, Update 1 of: electrophilicity index, *Chem. Rev.*, 2007, **107**, PR46–PR74.
22 E. P. Hunter and S. G. Lias, Evaluated gas phase basicities and proton affinities of molecules: an update, *J. Phys. Chem. Ref. Data*, 1998, **27**, 413–656.
23 R. G. Pearson, Recent advances in the concept of hard and soft acids and bases, *J. Chem. Educ.*, 1987, **64**, 561.
24 R. G. Parr, R. A. Donnelly, M. Levy and W. E. Palke, Electronegativity: the density functional viewpoint, *J. Chem. Phys.*, 1978, **68**, 3801–3807.
25 R. G. Parr and W. Yang, Density functional approach to the frontier-electron theory of chemical reactivity, *J. Am. Chem. Soc.*, 1984, **106**, 4049–4050.
26 R. G. Pearson, Chemical hardness and density functional theory, *J. Chem. Sci.*, 2005, **117**, 369–377.
27 M. Abdallah, H. M. Altass, A. S. Al-Gorair, J. H. Al-Fahemi, B. A. A. L. Jahdaly and K. A. Soliman, Natural nutmeg oil as a green corrosion inhibitor for carbon steel in 1.0 M HCl solution: Chemical, electrochemical, and computational methods, *J. Mol. Liq.*, 2021, **323**, 115036.
28 Y. Hussein Azeez, R. Obaid Kareem, L. Omer Ahmed, R. Anwar Omer, K. Ahmed Othman and D. A. Safin, Combined DFT and Monte Carlo simulation studies of potential corrosion inhibition properties of heterocyclic derivatives with an extended π-System, *Comput. Theor. Chem.*, 2024, **1240**, 114803.
29 A. Kasprzhitskii and G. Lazorenko, Corrosion inhibition properties of small peptides: DFT and Monte Carlo simulation studies, *J. Mol. Liq.*, 2021, **331**, 115782.
30 R. Abdel-Hameed, N. M. Abourashed, A. Hegazy, O. A. O. Alshammari, F. Alshammary, K. D. Alanazi, B. H. alshammari, T. Y. A. alanazi, A. H. Tantawy, D. F. Seyam and K. A. Soliman, Gemini cationic pyridinium surfactants based on palm kernel oil mucilage as novel green corrosion inhibitors for pipeline steel in aerated 0.5 wt% NaCl solution under dynamic conditions: Experimental and computational studies, *J. Mol. Liq.*, 2025, **429**, 127631.
31 I. B. Obot, D. D. Macdonald and Z. M. Gasem, Density functional theory (DFT) as a powerful tool for designing new organic corrosion inhibitors. Part 1: An overview, *Corros. Sci.*, 2015, **99**, 1–30.
32 H. M. Abd El-Lateef and A. H. Tantawy, Synthesis and evaluation of novel series of Schiff base cationic surfactants as corrosion inhibitors for carbon steel in acidic/chloride media: Experimental and theoretical investigations, *RSC Adv.*, 2016, **6**, 8681–8700.
33 S. Hamza, S. Shahen, A. M. Abdel-karim, A. A. El-Rashedy and A. M. Hyba, Eco-friendly corrosion inhibitor chitosan methionine for carbon steel in 1 M hydrochloric acid solution: experimental and theoretical approach, *Sci. Rep.*, 2025, **15**, 15924.
34 A. A. Al-Amiery, F. A. Binti Kassim, A. A. H. Kadhum and A. B. Mohamad, Synthesis and characterization of a novel eco-friendly corrosion inhibition for mild steel in 1 M hydrochloric acid, *Sci. Rep.*, 2016, **6**, 19890.
35 S. Monaci, A. Mezzetta, L. Guazzelli, D. Mecerreyes, M. Forsyth and A. Somers, Lignin-Based Bio Ionic Liquids for Enhanced Corrosion Protection of Metals, *ACS Sustain. Chem. Eng.*, 2025, **13**, 2023–2037.
36 A. C. Mureșan, D. L. Buruiana, V. Ghisman, E. E. Herbei and N. Bogatu, Corrosion Behavior of S235JR Carbon Steel in 0.5 M HCl Solution During 24 Weeks, *Metals*, 2025, **15**, 1092.
37 R. Dennington, T. A. Keith and J. M. Millam, *GaussView 6.0. 16*, Semichem Inc., Shawnee Mission, KS, USA, 2016, pp. , pp. 143–150.

38 M. J. Frisch, G. W. Trucks, H. B. Schlegel, G. E. Scuseria, M. A. Robb, J. R. Cheeseman, G. Scalmani, V. Barone, G. A. Petersson, H. Nakatsuji, M. Caricato, X. Li, H. P. Hratchian, A. F. Izmaylov, J. L. Sonnenberg, M. Hada, M. Ehara, K. Toyota, R. Fukuda, J. Hasegawa, M. Ishida, T. Nakajima, Y. Honda, O. Kitao, H. Nakai, T. Vreven, J. A. Montgomery, J. E. Peralta, F. Ogliaro, M. Bearpark, J. J. Heyd, E. Brothers, K. N. Kudin, V. N. Staroverov, R. Kobayashi, J. Normand, K. Raghavachari, P. G. Rendell, J. C. Burant, S. S. Iyengar, J. Tomasi, M. Cossi, N. Rega, J. M. Millam, M. Klene, J. E. Knox, J. B. Cross, V. Bakken, C. Adamo, J. Jaramillo, R. Gomperts, R. E. Stratmann, O. Yazyev, A. J. Austin, R. Cammi, C. Pomelli, J. W. Ochterski, R. L. Martin, K. Morokuma, V. G. Zakrzewski, G. A. Voth, P. Salvador, J. J. Dannenberg, S. Dapprich, A. D. Daniels, O. Farkas, J. B. Foresman, J. V. Ortiz, J. Cioslowski and D. Fox, *Gaussian 09 Rev. D.01*, Wallingford, CT, 2009.

39 M. Garcia-Ratés and F. Neese, Effect of the Solute Cavity on the Solvation Energy and its Derivatives within the Framework of the Gaussian Charge Scheme, *J. Comput. Chem.*, 2020, **41**, 922–939.

40 A. Ait Mansour, M. R. Al-hadeethi, H. Lgaz, K. Subbiah, M. Messali, H.-s. Lee, L. Bazzi and R. Salghi, Exploring the potential of isonicotinohydrazide derivatives in N80 steel corrosion control: An integrated approach through synthesis, modeling, and experimentation in acidic environments, *Colloids Surf., A*, 2023, **679**, 132542.

41 H. Sun, P. Ren and J. Fried, The COMPASS force field: parameterization and validation for phosphazenes, *Comput. Theor. Polym. Sci.*, 1998, **8**, 229–246.

42 R. Unissa, K. M. Younes, M. E. Osman, W. M. Khojali, M. D. Alshammari, H. Banu, R. Abdel-Hameed, A. H. Tantawy and D. R. A. Haleem, Green dual-action potential of newly synthesized sulfonamide-based ionic liquids: larvicidal activity against Culex pipiens and purification of oil-polluted water, *RSC Adv.*, 2025, **15**, 45707–45718.

43 K. Shalabi, A. Helmy, A. El-Askalany and M. Shahba, New pyridinium bromide mono-cationic surfactant as corrosion inhibitor for carbon steel during chemical cleaning: Experimental and theoretical studies, *J. Mol. Liq.*, 2019, **293**, 111480.

44 A. Abd-ElHamid, W. El-Dougdoug, S. Syam, I. Aiad, S. M. Shaban and D.-H. Kim, Synthesis of gemini cationic surfactants-based pyridine Schiff base for steel corrosion and sulfate reducing bacteria mitigation, *J. Mol. Liq.*, 2023, **369**, 120890.

45 M. Zeariya, F. Almarshadi, N. E. Elhassan, M. Humaida, M. Essa, A. Yousif, S. El-Shennawy, R. Abdel-Hameed, L. M. Reda and A. M. Metwally, Creating novel green synthesized cationic polymeric surfactants for removing the petroleum films from water surface: Surface-active and biological assessments, *J. Mol. Liq.*, 2025, 128164.

46 M. D. Alshammari, R. A. Hameed, K. M. Younes, A. Alshammari, A. M. Ashmawy and M. Deyab, Exploring Cationic Surfactant Mixtures: Electrochemical and Quantum Chemical Insights into Corrosion Mitigation of Carbon Steel in Acidic Conditions, *Colloids Surf., A*, 2025, 137383.

47 S. S. Subramaniyam, S. Rao, P. Rao, M. Sali, P. G. Krishna and K. Asha, An overview of corrosion and its control by the surfactants: a mini-review, *Can. Metall. Q.*, 2025, 1–31.

48 M. Abdallah, M. Alfakeer, F. H. Al-abdali, M. Sobhi, H. Hawsawi, D. F. Seyam, S. S. Al-Juaid and R. S. Abdel Hameed, Insights into the effectiveness of natural Mentha oil in mitigating the corrosion of carbon steel in sulfuric acid, *Green Chem. Lett. Rev.*, 2025, **18**, 2527724.

49 A. A. Ali, N. G. Gayash and D. F. Seyam, Isolation of Cinnamaldehyde and its application as a green corrosion inhibitor for A03081 alloy in 2.0 M HCl solution: Theoretical, Electrochemical and Thermodynamics studies, *Egypt. J. Chem.*, 2025, **68**, 703–713.

50 M. Abdallah, A. S. Al-Gorair, H. Hawsawi, F. Al-abdali, D. F. Seyam, S. S. Al-Juaid, E. Elmossalamy, R. S. A. Hameed, K. Soliman and M. Motawea, Assessment of quinazoline derivatives as efficient corrosion inhibitor for carbon steel in acidic environment. A theoretical and practical analysis, *Int. J. Electrochem. Sci.*, 2025, **20**, 100990.

51 M. Eissa, S. Etaiw, E. El-Waseef, A. El-Hossiany and A. Fouda, The impact of environmentally friendly supramolecular coordination polymers as carbon steel corrosion inhibitors in HCl solution: synthesis and characterization, *Sci. Rep.*, 2024, **14**, 2413.

52 L. K. Goni, S. A. Ali, H. A. Al-Muallem and M. A. J. Mazumder, Synthesis of a new quaternary ammonium salt for efficient inhibition of mild steel corrosion in 15% HCl: Experimental and theoretical studies, *Heliyon*, 2024, **10**.

53 S. Gao, Y. Huang, Y. Xiong, X. Guo, J. Zhang and L. Wang, Assessment of corrosion inhibition performance of quaternary ammonium based dicationic ionic liquids for AZ91D magnesium alloy in NaCl solution, *J. Mol. Liq.*, 2023, **386**, 122467.

54 C. Verma, M. Quraishi and K. Rhee, Hydrophilicity and hydrophobicity consideration of organic surfactant compounds: Effect of alkyl chain length on corrosion protection, *Adv. Colloid Interface Sci.*, 2022, **306**, 102723.

55 M. Zunita, D. Wahyuningrum, Buchari, B. Bundjali, I. G. Wenten and R. Boopathy, Corrosion inhibition performances of imidazole derivatives-based new ionic liquids on carbon steel in brackish water, *Appl. Sci.*, 2020, **10**, 7069.

56 P. Wang, D. Zhang, R. Qiu, J. Wu and Y. Wan, Super-hydrophobic film prepared on zinc and its effect on corrosion in simulated marine atmosphere, *Corros. Sci.*, 2013, **69**, 23–30.

57 A. Elaraby, D. F. Seyam and S. A. Abdelkader, Multidimensional insights of electrochemical and quantum investigations of morpholinium cationic surfactants as corrosion inhibitors for carbon steel in acidic solution, *Sci. Rep.*, 2025, **15**, 20175.

58 H. Jafari and E. Ameri, Synthesis and evaluation of Schiff base as corrosion inhibitor for carbon steel in 1 M HCl solution, *Anti-Corros. Methods Mater.*, 2024, **71**, 632–639.

59 M. Abdallah, M. Alfakeer, R. N. Felaly, A. M. Almohyawi, J. H. Al-Fahemi, S. S. Al-Juaid, D. F. Seyam, E. M. Mabrouk and K. A. Soliman, Evaluation of porphyrin molecules as effective corrosion inhibitors for copper alloy in sulfuric acid using both experimental and computational approaches, *J. Electrochem. Sci. Eng.*, 2025, **15**.

60 Q. Wang, X. Zhou, X. Sun, Q. Zhang, R. Wang, J. Zhao, R. Aslam, Y. Sun, Z. Yan and X. Li, Seaweed extract as green corrosion inhibitor for carbon steel in hydrochloric acid solution, *Colloids Surf., A*, 2024, **700**, 134751.

61 M. Swathika, K. R. Singh, M. Mehala, S. Pandey, J. Singh, R. P. Singh and A. Natarajan, Design and synergistic effect of nano-sized epoxy-NiCo 2 O 4 nanocomposites for anticorrosion applications, *RSC Adv.*, 2022, **12**, 14888–14901.

62 N. Arrousse, Y. Fernine, N. Al-Zaqri, A. Boshaala, E. Ech-Chihbi, R. Salim, F. El Hajjaji, A. Alami, M. E. Touhami and M. Taleb, Thiophene derivatives as corrosion inhibitors for 2024-T3 aluminum alloy in hydrochloric acid medium, *RSC Adv.*, 2022, **12**, 10321–10335.

63 M. A. Amin, S. S. Abd El-Rehim, E. El-Sherbini and R. S. Bayoumi, The inhibition of low carbon steel corrosion in hydrochloric acid solutions by succinic acid: Part I. Weight loss, polarization, EIS, PZC, EDX and SEM studies, *Electrochim. Acta*, 2007, **52**, 3588–3600.

64 O. Kharbouch, K. Dahmani, I. Saber, M. El-alouani, N. Errahamany, F. El Hajri, M. Galai, S. Boukhris, M. E. Touhami and H. Nassali, A multianalytical approach to benzodiazepine derivatives for the corrosion protection of mild steel in HCl solutions: Electrochemical analysis, SEM/EDX, XPS, DFT, and MDS calculations, *Asia Pac. J. Chem. Eng.*, 2025, **20**, e3164.

65 H. Zgueni, M. E. Mesky, N. Idlahoussaine, B. Ait Haddou, M. Znini, A. Oubair, E. H. Mabrouk, B. El Ibrahimi and D. Chebabe, Synthesis of a new benzimidazole surfactant as a new effective corrosion inhibitor for carbon steel in 1 M HCl acid medium: Experimental, surface morphological (SEM-EDX) and computational analysis, *J. Mol. Struct.*, 2025, **1345**, 143175.

66 A. S. Al-Gorair, R. Felaly, N. Fouad, S. S. Al-Juaid, D. F. Seyam, N. Saadan, A. Y. El-Etre, E. M. Mabrouk and M. Abdallah, Corrosion kinetics of carbon steel in hydrochloric acid and its inhibition by recycling Salbutamol extracted from expired Farcolin drug, *Green Chem. Lett. Rev.*, 2024, **17**, 2413418.

67 J. B. Benziger and L. R. Larson, An infrared spectroscopy study of the adsorption of CO on Fe/MgO, *J. Catal.*, 1982, **77**, 550–553.

68 E. Guglielminotti, Spectroscopic Characterization of the Fe/ZrO2 System: 1. CO Adsorption, *J. Phys. Chem.*, 1994, **98**, 4884–4891.

69 R. A. El-Nagar, N. Khalil, Y. Atef, M. I. Nessim and A. Ghanem, Evaluation of ionic liquids based imidazolium salts as an environmentally friendly corrosion inhibitors for carbon steel in HCl solutions, *Sci. Rep.*, 2024, **14**, 1889.

70 A. Toghan, H. Gadow, A. Fawzy, H. Alhussain and H. Salah, Adsorption mechanism, kinetics, thermodynamics, and anticorrosion performance of a new thiophene derivative for C-steel in a 1.0 M HCl: experimental and computational approaches, *Metals*, 2023, **13**, 1565.

71 K. Belal, A. El-Askalany, E. A. Ghaith and A. Fathi Salem Molouk, Novel synthesized triazole derivatives as effective corrosion inhibitors for carbon steel in 1M HCl solution: experimental and computational studies, *Sci. Rep.*, 2023, **13**, 22180.

72 E. Ituen, V. Mkpenie, S. Shaibu, L. Yuanhua, U. Inyang, S. Sun, S. Nelana, M. Klink and O. Ayanda, Evaluating the Potential of Ataluren as X80 Steel Corrosion Inhibitor in Acid Wash Solution: An Experimental and Computational Intelligence Approach, *Corros. Sci. Technol.*, 2025, **24**, 134–150.

73 E. Ech-chihbi, R. Bouzammit, R. Salim, M. Er-rajy, R. Salghi, K. Azgaou, M. Ouakki, K. Azzaoui, W. Ettahiri, A. S. Alanazi, G. A. Houari and B. Hammouti, Chromone-isoxazole derivatives as corrosion inhibitors for mild steel in 1 M HCl solution: Experimental, DFT and DFTB approaches, *Colloids Surf., A*, 2025, **720**, 137169.

74 I. Ghouafria, A. R. Nadji, B. Bezzina, H. Ferkous, N. Bengourna, H. Tahraoui, A. Amrane, A. Delimi, C. Boulechfar and A. Kahlouche, Sustainable corrosion protection: Unveiling Cystoseira sedoides as a high-performance green inhibitor for carbon steel: Experimental and computational studies, *Mater. Today Commun.*, 2025, **47**, 112900.

75 M. Er-rajy, S. Mujwar, H. Imtara, S. Z. Alshawwa, F. A. Nasr, S. Zarougui and M. Elhallaoui, Design of novel anti-cancer agents targeting COX-2 inhibitors based on computational studies, *Arab. J. Chem.*, 2023, **16**, 105193.

76 R. A. Costa, P. O. Pitt, M. L. B. Pinheiro, K. M. Oliveira, K. S. Salomé, A. Barison and E. V. Costa, Spectroscopic investigation, vibrational assignments, HOMO-LUMO, NBO, MEP analysis and molecular docking studies of oxoaporphine alkaloid liriodenine, *Spectrochim. Acta, Part A*, 2017, **174**, 94–104.